Investigating the impact of diffraction on GNSS carrier phase measurements

Journal of Geodesy (2026) 100:25
https://doi.org/10.1007/s00190-026-02045-w

ORIGINAL ARTICLE

Investigating the impact of diffraction on GNSS carrier phase measurements

Uttama Dutta[1,2] · Jan Johansson[1,2] · Rüdiger Haas[1]

Received: 27 August 2025 / Accepted: 21 February 2026

Abstract

This study investigates signal diffraction as a significant, yet often unmodeled, error source in high-precision Global Navigation Satellite Systems (GNSS), which typically rely on carrier phase measurements for sub-centimeter accuracy. While standard post-processing mitigates major errors like orbits, clocks and atmospheric delays, localized effects such as diffraction remain a challenge. Diffraction introduces a slowly varying, systematic bias into the measurements, which degrades the accuracy of high-precision positioning. The error is deterministic and structured, meaning it cannot be averaged out and requires physical or empirical modeling. By analyzing double-difference carrier phase residuals, precise point positioning (PPP) position estimates and signal-to-noise ratio (SNR) measurements from both long-term real and synthetically modified datasets, the research demonstrates that diffracted signals are indeed received in areas obstructed from direct satellite line of sight. These bent signals, when inadvertently included in positioning solutions, introduce significant errors that standard algorithms fail to correct, as they are highly dependent on the antenna's immediate local environment. Our simulation results show that the scatter of the position estimates can get twice as large or even more in the presence of non-minimal diffraction effects. A similar degradation can be seen from the analysis of real data, underscoring that diffraction is a critical factor potentially compromising the utmost accuracy of precise GNSS applications.

Keywords GNSS · Diffraction · Multipath · NLOS · PPP · RTK · SNR

1 Introduction

Present-day GNSS offers a variety of signals and frequencies to choose from and is used in various precise positioning applications, including monitoring of the earth with the help of International GNSS Service (IGS) and other permanent GNSS stations etc. GNSS provides continuous availability of data over a wide ground station network around the globe and together with other geodetic techniques contributes to the development of the International Terrestrial Reference Frame (ITRF) (Altamimi et al. 2023; IGS 2025). By using advanced techniques, such as precise point positioning (PPP), or real-time kinematic (RTK) positioning, or a combination of both, the GNSS positioning accuracy can be enhanced to centimeter level. However, the performance of GNSS, like any other technique, is prone to error sources. These error sources can originate from various segments. Atmospheric errors may arise from the troposphere or ionosphere. Space segment errors include issues related to satellite orbits, clock inaccuracies, antenna center variations, relativistic effects and phase windup. Meanwhile, user segment errors can stem from diffraction, multipath effects, antenna phase center variations, receiver clock errors and noise. The majority of these error sources can be rigorously modeled using established physical and statistical frameworks and are typically mitigated through specialized scientific post-processing software such as Bernese GNSS software (BSW, Dach et al., 2015) or GipsyX software (Bertiger et al. 2020). However, signal degradation due to fading caused by the local environment around the antenna continues to pose a problem. It is seen

✉ Uttama Dutta
uttama@chalmers.se

Jan Johansson
jan.johansson@chalmers.se

Rüdiger Haas
rudiger.haas@chalmers.se

[1] Department of Space, Earth and Environment, Chalmers University of Technology, 41296 Gothenburg, Sweden

[2] Department of Measurement Science and Technology, RISE Research Institutes of Sweden, Brinellgatan 4, 50462 Borås, Sweden

Published online: 02 April 2026

that not only reflections but also diffraction from surrounding objects interfere with the line-of-sight GNSS signal, degrading the positioning accuracy even in a post-processing mode.

Typically, in geometrically challenging situations, such as, e.g., a so-called urban canyon, GNSS receivers lack a clear line-of-sight (LOS) to the satellite even at very high elevations. A similar challenge arises in the context of construction equipment operating in environments such as mines, where GNSS signals are frequently obstructed or reflected. These signal disruptions are caused not only by surrounding infrastructure but also by the metallic structure of the machinery itself, such as in excavators. Typically, the GNSS antenna receives a composite signal comprising both a direct line-of-sight component and multiple reflected or diffracted components from nearby surfaces, introducing significant errors in the GNSS measurements, often resulting in substantial positioning inaccuracies.

GNSS measurements are interfered when the LOS signal is close to an obstruction such as the sharp edge of a wall due to signal bending or diffraction effect (Bradbury 2007; Dutta and Johansson 2023). Such effects occur in the vicinity of the obstruction and introduce decimeter–centimeter levels of delay in range measurements (McGraw et al. 2020). This can significantly degrade the GNSS signal resulting in poor positioning performance, especially in dense urban areas (Zhang and Hsu 2021).

Diffraction can cause rapid phase fluctuations with significant amplitude attenuation and may also introduce cycle slips (Breitsch et al. 2020). Schaper et al. (2022) showed that diffraction affects all types of signal classes, resulting in an extra path delay which is usually in the centimeter-range and a loss of signal strength of upto 17 dB-Hz. Zhang and Hsu (2021) assessed the performance of diffraction models such as knife edge and UTD (Uniform Geometrical Theory of Diffraction) on experimental data by simulating carrier to noise ratio and pseudorange. UTD and the 3D building model to evaluate the diffraction effect have also been explored elsewhere (Fan and Ding 2006; Nicolás et al. 2012; Panicciari et al. 2017; Suzuki and Kubo 2012).

Brunner et al. (1999) developed a stochastic SIGMA-Δ model for GPS signal diffraction. They use signal-to-noise ratio (SNR) as their primary parameter for demonstration of diffraction. Xi et al. (2023) and Zimmermann et al. (2017) used obstruction-adaptive elevation masks (OAEMs) to study GNSS signal diffraction. Xi et al. (2023) concluded that diffraction impacts can be much larger than multipath. It can reach a magnitude of several carrier wavelengths and can have various patterns, trend, period and regular or irregular fluctuations. Therefore they concluded that diffraction can be even more difficult to mitigate than multipath. They also concluded that OAEMs can weaken the geometry and thus the obtained position solution. Therefore, use of OAEMs may not always be the best approach. Zou et al. (2023) developed two strategies for implementing a multi-point hemispherical grid model. They concluded that strategy-1 of eliminating non-line-of-sight (NLOS) signals can lead to poor satellite geometry and they recommended down-weighting the NLOS signal observations as their strategy-2.

Zhang et al. (2022) proposed a composite stochastic model based on elevation, azimuth and carrier-to-noise-power-density ratio (C/N0), which can reflect the terrain topography of the monitoring station. They introduced a geographic, azimuth-dependent cutoff elevation to detect and exclude the NLOS reception. A similar strategy was also used by Ren et al. (2023) who proposed a multipath hemispherical map model with geographic cutoff elevation constraints, which considers signal quality and terrain topography surrounding the station to mask the unsatisfactory NLOS signals. Jiang and Groves (2014) explored the potential of using dual-polarization antenna technology for detecting and mitigating the reception of NLOS signals and severe multipath interference. Groves and Adjrad (2017) demonstrate a likelihood-based 3D-mapping-aided GNSS ranging algorithm that enables NLOS signals prediction to contribute to the position solution without explicitly computing the additional path delay due to NLOS reception. Groves and Jiang (2013) investigated multiple techniques for mitigating the impact of NLOS reception and multipath interference on position accuracy. They also pointed out that consistency checking using a conventional sequential elimination technique was found to degrade horizontal positioning performance by 60 % because it often eliminated the wrong measurements in cases when multiple signals were affected by NLOS reception or strong multipath interference. Xi et al. (2025) proposed a method for extracting and modeling diffraction error, contributing valuable empirical insights into its time-varying characteristics. Their work quantitatively demonstrated that diffraction error often follows a monotonic trend and can reach significant amplitudes of 50 to 200 millimeters, highlighting its potential impact on precise positioning. However, their approach is primarily based on geometrical modeling and does neither integrate the foundational physics of diffraction nor utilize supportive metrics like signal-to-noise ratio (SNR) in its analysis. Certain aspects of their vertical diffraction model, invite further investigation. For example, their model suggests a significant increase in error magnitude with the horizontal distance (S) to the obstruction. Without specific geometric constraints, this relationship could be misinterpreted, as it contrasts with the expectation that nearby obstructions typically pose a greater threat. Additionally, their suggestion that vertical diffraction error is larger for high-elevation satellites than for low-elevation ones—under identical S and diffraction angles—presents a finding that appears to contradict general diffraction theory and observational experience, where lower-elevation signals are more vulnerable. These points of

divergence underscore the complexity of modeling diffraction and identify a clear need for models more deeply rooted in wave propagation physics.

Thus, despite some progress, there is a notable gap in recent literature that isolates diffraction from other local environment-based signal degradation phenomena such as multipath. In high-precision real-time GNSS applications, an elevation cutoff angle of 10 to 15° is typically used. Users, such as those operating machine guidance systems, rely on GNSS data every second. However, surrounding objects, including the machine itself, often cause multipath and diffraction effects. These disturbances can result in coordinate errors of several centimeters or even decimeters. Multipath interference is a well-known challenge for moving or rotating construction equipment like excavators and cranes. Diffraction, on the other hand, is either overlooked or not well understood. Although typically short-lived, diffraction can significantly impact the accuracy of RTK and Network RTK (NRTK) measurements. Most modern studies treat diffraction as part of a broader urban signal degradation model and diffraction-specific research and modeling remains underdeveloped. Further empirical studies are needed to isolate diffraction effects and quantify their impact independently from other signal disturbances.

This study investigates GNSS signal diffraction through a multi-faceted approach grounded in a simple geometric model and the underlying wave physics, which also informs our modeling of Signal-to-Noise Ratio (SNR) measurements. To systematically evaluate the impact of an obstruction's proximity, our simulation methodology introduces a virtual obstruction at half the distance of the documented real-world obstacle, thereby providing a comparative analysis of diffraction effects at two distinct ranges. We investigate the effects of diffraction on dual-frequency PPP positioning as well as double-differentiated single-frequency carrier phase residual analysis. Our analytical approach utilizes standard, widely available scientific post-processing software (Bernese and GipsyX software). We avoid position estimation using double differences, as compared to the process employed by Xi et al. (2025). This methodological selection is critical; by avoiding the estimation of the numerous parameters inherent in network adjustments, we ensure that the diffraction-induced error signature remains distinctly preserved within the carrier phase residuals. In contrast to the theoretical extraction techniques noted in prior work, our method offers a more direct pathway to observing the phenomenon. To ensure transparency and reproducibility, we provide a complete outline of our PPP positioning and double-difference residual analysis procedure. Furthermore, the robustness of our findings is strengthened by a comprehensive two-month data analysis period, significantly longer than the short-term (e.g., one-day) datasets often used for validation. The impact of diffraction is corroborated through multiple, independent lines of evidence: the analysis of Signal-to-Noise Ratio (SNR) measurements from real data and precise LiDAR-scanned environmental data, which collectively confirm that the anomalies observed in the residuals are directly attributable to physical diffraction from the obstruction.

The paper is organized as follows. Section 2 delves into the details of the theoretical background of the paper. Section 2.1 discusses the modeling of loss in signal strength due to diffraction using a Knife Edge model, while Sect. 2.2 provides a background on signal diffraction study using carrier phase residuals. Section 3 presents the results in two parts. Section 3.1 focuses on the results of a simulation study performed on the ONSA-ONS1 baseline. These results show a clear signature in the double-difference residuals and a degradation of the position estimates when a wall is simulated around one of the stations (ONSA), causing simulated diffraction effects. This section is necessary to understand what one can expect from real measurements. The process and the settings used in this section for obtaining the BSW residuals and the GipsyX position estimates remain exactly the same when demonstrating the impact on real data in the next section. This is followed by Sect. 3.2 which presents the results of studies performed on the POS1–POS2 baseline, where one station (POS1) experiences real diffraction effects. Section 4 discusses the various interesting findings in detail and explains how they can be interpreted. Section 5 presents the conclusions of the work and also discusses some future possibilities for research on GNSS diffraction.

2 Theoretical background

The accuracy of GNSS is fundamentally governed by signal propagation effects, chief among them being Fresnel zone clearance and diffraction. The First Fresnel Zone defines an ellipsoidal volume around the direct satellite receiver path where most signal energy propagates; obstructions within this zone cause signal attenuation and phase shifts. When a signal encounters such an obstacle, diffraction occurs, bending the wavefront and introducing a non-line-of-sight (NLOS) component characterized by group delay and amplitude loss. The receiver misinterprets this delayed path as a longer pseudorange, inducing significant positioning errors. In this section we take a look at the theoretical aspects behind the diffraction effects caused by an obstruction (a wall) on the GNSS signals. While the signal strength obtained from satellites is an indicator of the diffraction effects, diffraction can also be studied using the difference in path length/range measurements between the Shortest Geometric Path (SGP) and the diffracted NLOS path to the satellite. The results obtained in this paper use signal strength measurements, range residuals and position estimates to demonstrate the effect produced

by a diffracting wall both using simulations as well as real data.

2.1 Modeling signal diffraction effects on SNR and range measurements

Radio signals can reach receivers without a direct line of sight via mechanisms like reflection and diffraction. Diffraction, explained by Huygens' Principle, allows waves to bend around obstacles by treating each point on a wavefront as a source of new wavelets. We model this using knife edge diffraction, where an obstruction is simplified to a sharp, impenetrable edge. The field at the receiver is found by summing the wavelets from all secondary sources above this edge, assuming polarization remains unchanged. This provides a conservative estimate of real-world diffraction. Diffraction effects in this work are studied using the knife edge diffraction model (KED) (Orfanidis 2002).

The diffraction coefficient is the ratio of diffracted field to the free space field. For the KED model it is given as (Equation 17.14.1 in Orfanidis (2002))

$$D(\nu) = \frac{1}{1-j}[F(\nu) + \frac{1-j}{2}], \tag{1}$$

where j is the complex variable and $F(\nu)$ is the Fresnel integral which integrates the contribution of all the secondary sources and is given as (Equation 17.13.13 in Orfanidis (2002))

$$F(\nu) = \int_0^{\nu} e^{-j\pi u^2/2}\, du, \tag{2}$$

where u is the variable for integration and ν is the Fresnel–Kirchhoff diffraction parameter. For a given wavelength λ, ν can be computed as

$$\nu = h\sqrt{\frac{2(R_1+R_2)}{\lambda R_1 R_2}}. \tag{3}$$

where R_1 and R_2 are the distances of the obstruction from the transmitting and receiving antenna, respectively (variables r_1 and r_2 from Fig. 17.14.3 (Orfanidis 2002)). h is the clearance height or the perpendicular distance between the LOS path and the knife edge of the obstruction. The value of h is negative if the knife edge is below the LOS path. However, as the satellite receiver geometry changes, the value of h becomes positive when the knife edge is above, thus obstructing the SGP.

From Eq. 1 one can compute the diffracted signal power as follows

$$|D(\nu)|^2 = 0.5|F(\nu) + \frac{1-j}{2}|^2. \tag{4}$$

Then the accurate value of diffraction loss (dB) can be written as

$$L = -10\log_{10}|D(\nu)|^2. \tag{5}$$

This is the amount of signal strength that is expected to be lost due to signal attenuation due to diffraction. When modeling the SNR, we subtract this loss from an 'open sky' SNR model to get a resultant SNR for the diffracted signal. This is shown in Sect. 3.2.4. An approximation of the above model for diffraction loss, also known as the Lee piece-wise model (Rappaport 1996), is given as follows:

$$L = \begin{cases} 0 & \text{for all } \nu \le -1 \\ 20\log_{10}(0.5 - 0.62\,\nu) & \text{for all } -1 \le \nu \le 0 \\ 20\log_{10}(0.5e^{-0.95\,\nu}) & \text{for all } 0 \le \nu \le 1 \\ 20\log_{10}\left(0.4 - \sqrt{0.1184 - (0.38 - 0.1\,\nu)^2}\right) & \text{for all } 1 \le \nu \le 2.4 \\ 20\log_{10}\left(\frac{0.225}{\nu}\right) & \text{for all } \nu \ge 2.4 \end{cases} \tag{6}$$

The knife edge model has also been used by Zhang and Hsu (2021) to understand the diffraction effects on GNSS signals. In this work, we make a similar effort to understand the signal degradation in the vicinity of a GNSS antenna with signal-to-noise ratio (SNR) measurements using this model.

In the case of GNSS, the distance to the satellite R_1 is much larger than R_2, the distance to the receiver shown in Fig. 1 as the receiving point P. Thus, Eq. 3 can be simplified to

$$\nu = h\sqrt{\frac{2}{\lambda R_0}}, \quad \text{where} \quad \frac{1}{R_0} = \frac{1}{R_1} + \frac{1}{R_2} \approx \frac{1}{R_2}. \tag{7}$$

Thus, one can compute the diffraction loss for a knife edge obstruction given the geometrical measurements R_0 and h for a specific receiver environment.

Figure 1a shows the side view of a typical knife edge diffraction environment near a GNSS antenna. The geometry in the vicinity of the GNSS antenna together with the NLOS and SGP path from a satellite at a specific azimuth is shown. From figure, the perpendicular distance between the SGP and the NLOS path, h, can be computed as

$$h = \Delta V\cos(\theta_o) = (V - d\,\tan(\theta_o))\,\cos\theta_o, \tag{8}$$

where (θ_o) is the elevation angle to the satellite from the receiver. Here θ is the elevation of the edge of the wall. For

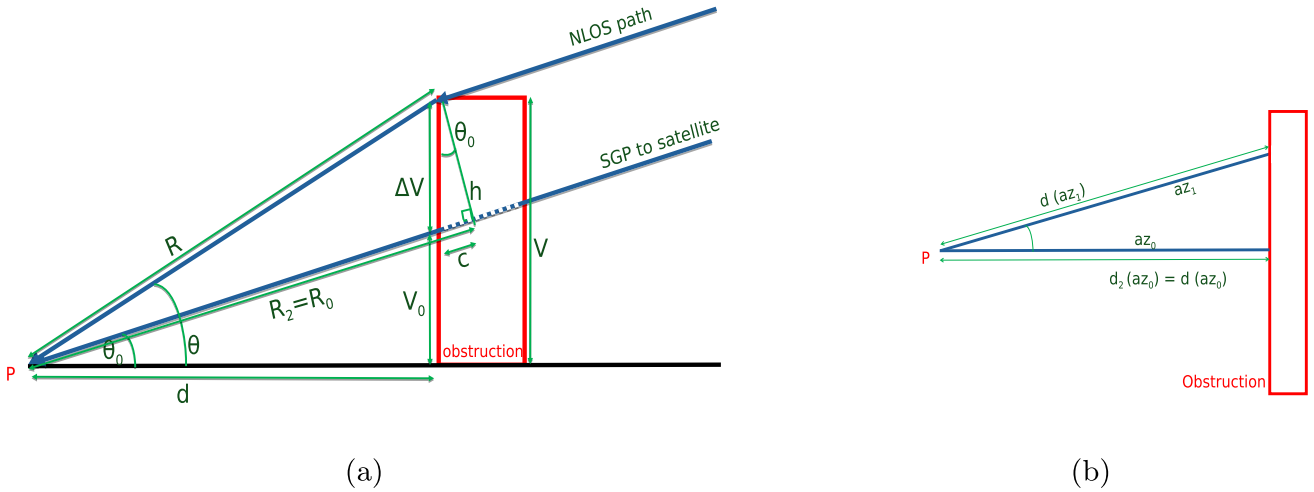

(a) (b)

Fig. 1 Example geometry of a diffraction environment around a GNSS antenna, **a** side view, **b** top view

the geometry of Fig. 1a, the difference in path length can be computed as shown in Dutta and Johansson (2023) by using the following equations:

$$\Delta V = V - d \cdot \tan(\theta_o) \quad \text{and} \quad c = \Delta V \cdot \sin(\theta_o) \tag{9}$$

$$R = \sqrt{V^2 + d^2} \quad \text{and} \quad R_o = \sqrt{(d \cdot \tan(\theta_o))^2 + d^2} + c \tag{10}$$

Thus, R_0 can be computed from the horizontal distance d. The difference between R and R_o is the path length difference.

Figure 1b is an example of the top view of such a setup shown in Fig. 1a. The signal could arrive from different directions, and therefore, the value of d changes with azimuth az. If the distance d at a reference azimuth az_0 is $d(az_0)$, then at an azimuth az_1, the new distance $d(az_1)$ is given as,

$$d(az_1) = \frac{d(az_0)}{\cos(az_1 - az_0)}. \tag{11}$$

For the geometrical relations shown in Fig. 1a, the expected extra path delay for varying elevations (θ and θ_0), horizontal distances to the wall (d) and for a constant wall height (V) of 0.85 m are shown in Table 1. In this case, the shortest distance to the wall is assumed to be 1.95 meter at an azimuth of 315° and this azimuth is also taken as a reference azimuth. The wall extends as an example from azimuth 240° to 360°. However, the first part of the table has 8 rows that show the path delays for azimuth between 240° to 310°. This is because the table is symmetric around the reference azimuth of 315° and the remaining rows can therefore be omitted. In the case of a circular wall, the parameter d does not have any azimuth dependence. In such a case, there is always a single value of θ. The path delays for such a geometry are shown in the last row of Table 1. The constant distance to the wall in this case is taken as 1 meter.

In the first column of Table 1 different values of d, based on different azimuth, for the reference azimuth of 315° are computed using Eq. 11. For these values of d and a constant value of $V = 0.85$ meter, the values of θ are computed. Varying values of θ_0 from 0° to θ were assumed for each value of d, and the corresponding delays were computed using Eqs. 9 and 10. As is clear from Table 1, the expected path delay ranges from millimeters to decimeters. With a lower-elevation angle (θ_0), the path difference/delay is larger. Also, the higher the azimuth separation from the reference azimuth, the lower the delay. This is because a larger azimuth separation from the reference azimuth implies that the value of d increases and if V is constant, θ decreases. Simply stated, as the wall moves further and further away, the shadow cast by it on the antenna is smaller and less impactful. A too large azimuth separation leads to a large path loss, and therefore the signal, if received, is weak enough to be rejected by the receiver.

It is important to understand how much impact the diffraction effect could have, based on the geometry of the environment. From Eq. 6 the value of diffraction loss is 0 for $\nu \leq -1$. Therefore, a critical value of h, which is h_c, below which minimal diffraction effects are seen to occur can be computed as

$$h_c = \sqrt{\frac{\lambda R_0}{2}}. \tag{12}$$

h can take both positive and negative values. The positive/negative sign of h, as mentioned before, simply indicates that the knife edge is above/below the SGP path, respectively. Thus, theoretically, if the value of h computed for a certain

Table 1 Path delay measurements for both azimuth-dependent and azimuth-independent cases

Path delay (m) when d is azimuth dependent											
Az/El (°)	0	2	4	6	8	10	12	14	16	18	20
240	0.048	0.023	0.007								
250	0.078	0.051	0.030	0.014	0.004						
260	0.105	0.077	0.054	0.034	0.019	0.009	0.002				
270	0.128	0.100	0.075	0.054	0.037	0.022	0.012	0.004	0.001		
280	0.147	0.119	0.094	0.071	0.052	0.036	0.022	0.012	0.005	0.001	
290	0.162	0.133	0.108	0.085	0.064	0.047	0.032	0.020	0.011	0.004	0.001
300	0.172	0.143	0.117	0.094	0.073	0.055	0.039	0.026	0.016	0.008	0.003
310	0.177	0.148	0.122	0.098	0.077	0.059	0.043	0.029	0.018	0.010	0.004

Path delay (m) when d is azimuth-independent										
El (°)	0	4	8	12	16	20	24	28	32	36
Delay	0.313	0.256	0.204	0.158	0.117	0.082	0.053	0.031	0.014	0.004

All values are in meters

receiver geometry is larger than h_c, diffraction loss is impacting the positioning performance of the receiver.

The larger the value of R_0 (which is a function of d and satellite elevation), the higher is the critical height h_c, and therefore, the smaller is the impact. Thus, as the receiver moves away from the wall, the diffraction impact due to the wall reduces. Also, as a satellite rises higher up in elevation, the first Fresnel zone of its SGP is no longer blocked or obstructed and the impact of diffraction reduces. The study of diffraction as a function of critical height and its variation with Fresnel zones in detail is beyond the scope of this work and will be studied as a future work. However, in this paper we discuss the implications of having an obstructed first Fresnel zone and interpret this using the parameters ν and h in Sect. 4.

2.2 Signal diffraction study with carrier phase residuals

The carrier phase observation (in meters) for dual-frequency GNSS can be written as

$$L^i_{1k} = \rho^i_k + T^i_k - I^i_k + c\delta_k - c\delta^i + \lambda_1 n^i_{1k} + MP^i_{1k}, \tag{13}$$

$$L^i_{2k} = \rho^i_k + T^i_k - \frac{f_1^2}{f_2^2} I^i_k + c\delta_k - c\delta^i + \lambda_2 n^i_{2k} + MP^i_{2k}, \tag{14}$$

where ρ^i_k is the geometric range to the satellite i from the receiver antenna k, T^i_k is the tropospheric error, I^i_k the ionospheric error, c the speed of light, δ_k the receiver clock correction, δ^i the satellite clock correction, λ the wavelength of the L_1 or L_2 carrier signal, n the respective carrier phase ambiguity and MP^i_{1k} denotes the local effects influenced by the environment around the antenna such as multipath and diffraction. Other biases, such as receiver noise, are neglected for the present study. As mentioned earlier, in this study we intend to point out the impact of diffraction and it is assumed for the sake of simplicity that receiver noise is much less impactful than diffraction. Since we use two Septentrio PolaRx5 receivers which are of the same make and model, in a double-difference mode, such an assumption is safe to make. Please find more details on the analysis of the quality of the receiver baseline using triple differences in Appendix Sect. 7.1.

The PPP technique, which uses dual-frequency measurements to form an ionosphere-free (L_3) combination, introduces uncertainties and may not be the most optimum method to isolate carrier phase diffraction. An alternate way of handling the error sources is to use double-differencing technique. Receivers located in the near vicinity (a few meters) of each other are usually affected by the atmosphere by similar amounts and can be considered co-located. Computing single differences between the carrier phase observations (defined in Eqs. 13 and 14) obtained from two such co-located receivers k and l for a single satellite i removes the effect of the clock error from the corresponding satellite as shown below:

$$L^i_{1kl} = \rho^i_{kl} + T^i_{kl} - I^i_{kl} + c\delta_{kl} + \lambda_1 n^i_{1kl} + MP^i_{1kl_y}, \tag{15}$$

$$L^i_{2kl} = \rho^i_{kl} + T^i_{kl} - \frac{f_1^2}{f_2^2} I^i_{kl} + c\delta_{kl} + \lambda_2 n^i_{2kl} + MP^i_{2kl}. \tag{16}$$

Double-difference computation between these single differences for satellites i and j, removes the effect of the receiver clock error. In addition, since stations k and l are co-located, variations in troposphere and ionosphere over these short distances can be neglected and the equations simplify to:

$$L^{ij}_{1kl} = \rho^{ij}_{kl} + \lambda_1 n^{ij}_{1kl} + MP^{ij}_{1kl}, \tag{17}$$

$$L_{2kl}^{ij} = \rho_{kl}^{ij} + \lambda_2 n_{2kl}^{ij} + M P_{2kl}^{ij}. \quad (18)$$

Thus, using double-difference carrier phase analysis for co-located GNSS stations simplifies the estimation problem and can be done using a single-frequency observable which minimizes the possibility of introducing unwanted uncertainties.

The Bernese GNSS software (Dach et al. 2015) carefully models all relevant systematic errors such as satellite orbits, clocks, propagation medium, relativistic effects, antenna phase center variations, etc. However, local un-modeled error sources such as fading due to multipath and diffraction which can be the cause of severe signal degradation cannot be catered to by such post-processing software as these error sources are largely dependent on the local environment around the receiver antenna. In this study we use double-difference residuals generated by the Bernese software version 5.4 for single-frequency observations derived from co-located stations to demonstrate the effect of diffraction primarily affecting one of these stations. GPSEST, part of the Bernese Processing Engine, estimates geodetic parameters from GNSS data, such as station coordinates, velocities, clocks, ambiguities, etc. To minimize parameter absorption of local unmodeled effects, double-difference residuals were computed by fixing station coordinates and disabling ionosphere and troposphere estimation. GPSEST produces an initial residual file, which is typically screened for outliers; however, all residual plots in this study use the first residuals without any outlier rejection.

3 Results

3.1 Simulation studies with ONSA

Local environmental effects on GNSS measurements are usually absorbed in the estimated parameters and remaining residuals. Thus, a suitable analysis strategy is needed to highlight these effects to their full extent. Dual-frequency PPP analysis is not well suited since diffraction is frequency-dependent, but PPP uses frequency combinations to remove ionospheric effects. Instead network processing of co-located stations with one-frequency data is more applicable. Provided that the station positions are well known, all parameters cancel out, except the phase ambiguities that still need to be estimated. The environmental effects will thus partly be absorbed in the ambiguity parameters, but primarily be visible in the residuals.

Before applying this analysis approach to the POS1 and POS2 stations that are located in a complicated environment on a roof top (see Sect. 3.2), we tested it with the two IGS (International GNSS Service) stations ONSA and ONS1 that are located in a much less complicated environment. We performed a simulation of diffraction effects due to a wall at 1 m distance from ONSA and then study the original ONSA-ONS1 data as well as the modified ONSA-ONS1 data. Similarly as for the later investigation of POS1 and POS2, the positions of ONSA and ONS1 were estimated beforehand.

3.1.1 The ONSA-ONS1 baseline

ONSA and ONS1 are co-located stations in about 59 m distance at the Onsala Space Observatory. We determined the coordinates of the two stations by analyzing 14 days data of ONSA and ONS1 using the software GipsyX (Bertiger et al. 2020). Data of GPS, GLONASS and Galileo with 300 s sampling were used to derive daily estimates of the station positions by applying the PPP analysis strategy with an elevation cutoff of 20°. The high-elevation cutoff ensured that we did not include degraded signals from lower-elevation observations for reference position estimates. The period August 11–24, 2023, was chosen since it was a period of low rainfall rate at Onsala in the summer of 2023. We focused on the dry days in order to avoid being impacted by potential multipath reflection effects due to wet bedrock around the two antennas. We used data from SMHI (SMHI 2025) and weather data recorded at the observatory to eliminate 'bad days'.

3.1.2 Post-processed range residuals for the ONSA-ONS1 baseline using a simulated wall

We performed a single-frequency double-differencing analysis with the BSW software for the ONSA-ONS1 baseline. The station coordinates were fixed to the values provided in Table 2, and only phase ambiguity parameters were estimated. No outlier rejection was performed. This analysis was done for the original ONSA-ONS1 data, as well for the modified ONSA-ONS1 data where the effects of a diffracting wall at 1 m distance from ONSA were simulated. This wall was simulated around ONSA between azimuth of $180^o - 270^o$ a constant horizontal distance $d = 1$ meter and extending 0.85 m above the height of the ONSA antenna, see Fig. 2.

The diffraction model presented in Dutta and Johansson (2023) was used to calculate the to be expected diffraction effect for GPS and Galileo satellites that were impacted by this simulated wall (that is those satellites appearing between azimuth of $180^o - 270^o$ and below an elevation of 40.3645^o). The difference in path length (see Eqs. 9 and 10) was then added for each of the impacted satellites to the corresponding L1C and L2W frequency carrier phase measurements (refer International and Service (2018)) in the ONSA RINEX files, while the data of all other satellites were kept as in the original RINEX file. The L1C (single) frequency double-difference residuals from analyzing the diffracted ONSA data together with the original ONS1 data are presented in Fig. 4a. The

Table 2 Repeatability expressed as root-mean-square (RMS) deviation of the results derived from GipsyX PPP analysis using GPS, GLONASS and Galileo data for 14 days (August 11–24, 2023)

Station name	RMS (mm)			Average ITRF20 coordinates (m)		
	X	Y	Z	X	Y	Z
ONSA	1.5	1.3	1.4	3370658.2820	711877.4093	5349787.1456
ONS1	1.0	1.3	1.9	3370666.6429	711819.1955	5349788.2708

The average coordinates (ITRF20) fixed for further BSW analysis are also shown

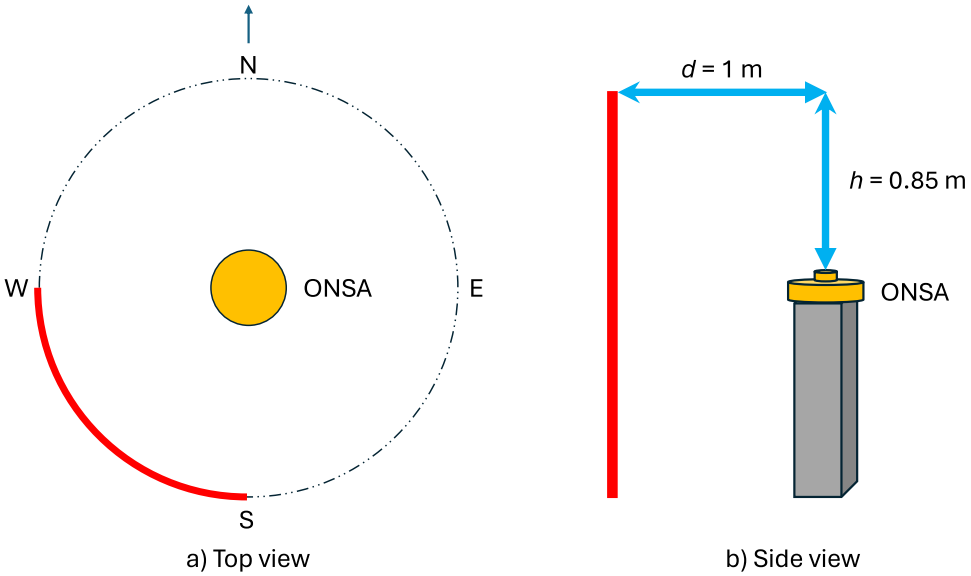

Fig. 2 Top view (left) and side view (right) of ONSA with a simulated wall, shown in red, at a horizontal distance of 1 m between azimuth of $180^o - 270^o$, extending 0.85 m above the height of the antenna

elevation cutoff angle used for this processing was 3^o. Figure 4a and b present double-difference residuals, but the azimuth and elevation angles in it are referenced to a single station–satellite pair. These correspond to the angles from the ONSA station to the second satellite in the pair. Since ONSA and ONS1 are co-located, their respective angles to any satellite are nearly identical.

The double-difference residuals depicted in Fig. 4a can be compared to those obtained by the same processing strategy (Fig. 3) but using the original RINEX files of both ONSA and ONS1, see Fig. 4b. The black rectangular window in both plots indicates the position of the simulated wall. The impact of diffraction is up to a few decimeters and can be compared with the theoretical values of path delay presented in Table 1. This definitely indicates that even for a differential solution of co-located stations, diffraction effects cannot be ignored for precise position estimation. Though we avoid estimation of most parameters, this is not simple forward modeling, since ambiguities still need to be estimated. The residual values of Fig. 4a are similar to the last row of Table 1; however, they are not exactly the same since we have two satellites and two receivers involved. While this figure demonstrates the impact of diffraction, it is also important since it can be used as a reference to understand the plots obtained in Figs. 8 and 9 for real data that were processed with the same analysis strategy.

3.1.3 Impact of diffraction on PPP position estimates of ONSA

The modified RINEX files of ONSA obtained in Sect. 3.1.2 were used to compute 5-minute position estimates using PPP analysis with the GipsyX software during the period of August 18-24, 2023. GPS and Galileo dual-frequency (L1C-L2W/ L1C-L5Q) observations were used for this processing, using an elevation cutoff angle of 3^o. Station positions were estimated with 5 min temporal resolution.

The derived position estimates were then compared to 5-minute GipsyX PPP position estimates obtained from the original ONSA data also with GPS and Galileo dual-frequency observations computed during the same period of time. Figure 5 shows plots of differential changes with respect to mean position estimates for ONSA in the east, north and up direction, respectively. Position estimates for modified and original observations of ONSA are compared. The corresponding RMS values are provided in figure legend. One can clearly see the large impact of signal diffraction due to the wall on position estimation.

Diffraction error can be distinguished from multipath. Diffraction causes frequent gross errors in positioning as shown by the sudden jumps in the position estimates. While carrier phase multipath is never larger than a quarter wavelength (Hofmann-Wellenhof et al. (2008)), diffraction can

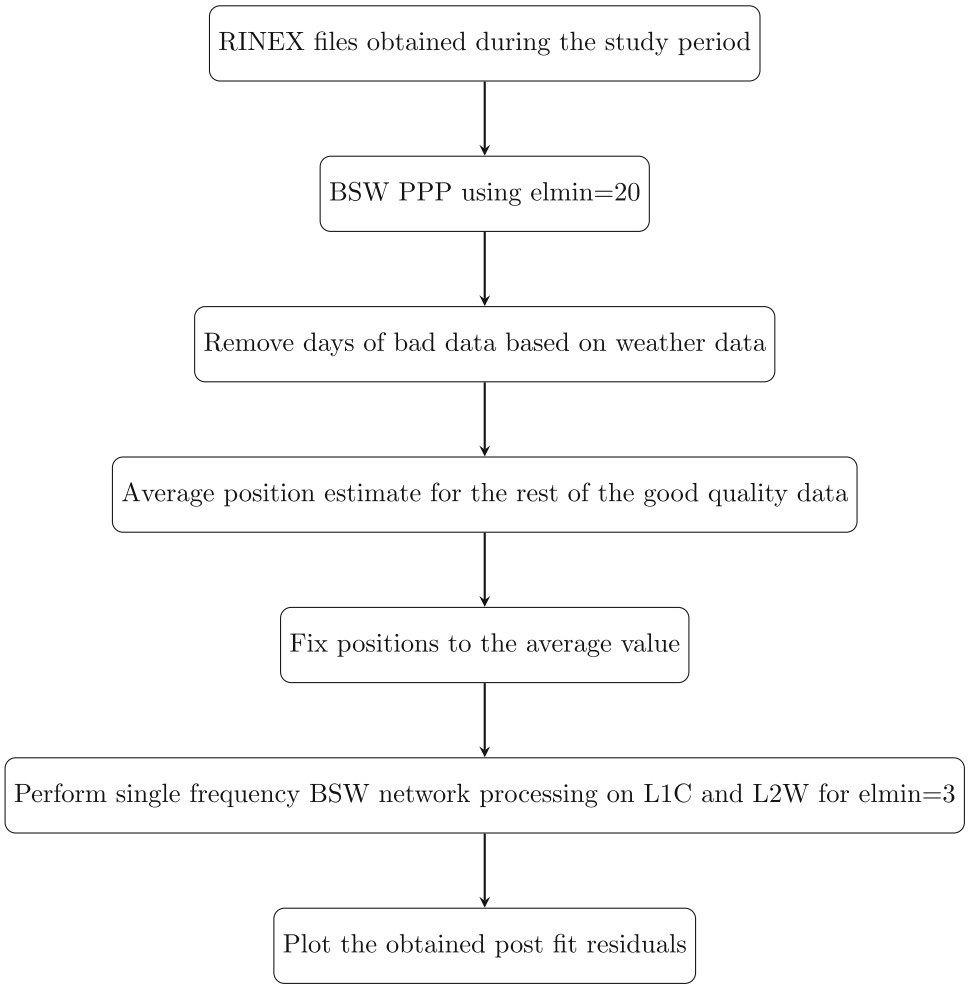

Fig. 3 Flow chart of the data processing

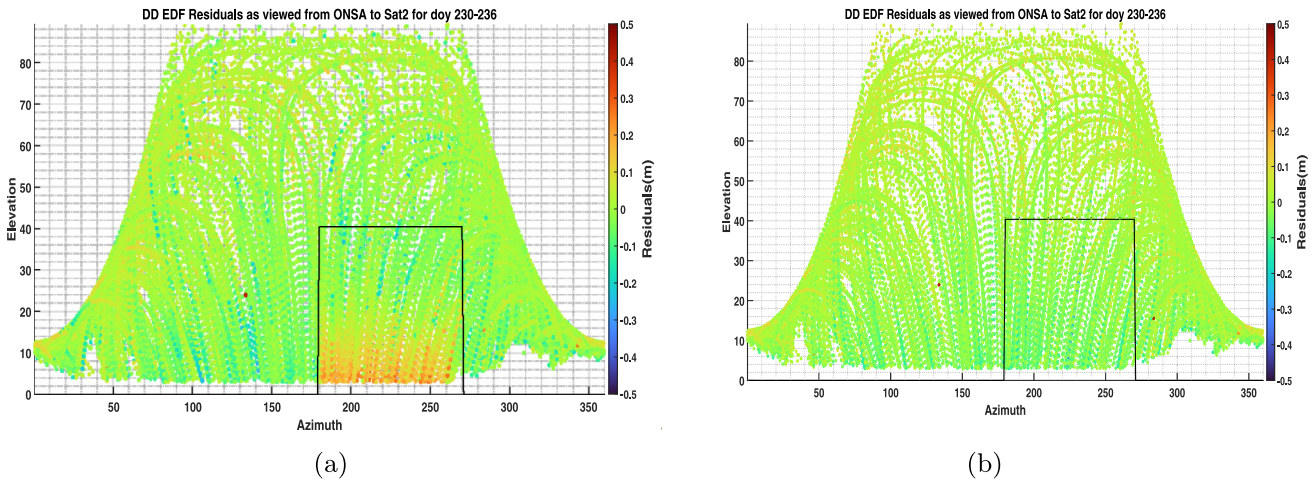

(a) (b)

Fig. 4 Double-difference residuals for the ONSA-ONS1 baseline based on a L1C analysis (GPS, GLONASS, Galileo) with the Bernese software for a 7-day period (August 18-25, 2023) using **a** modified ONSA RINEX data and the original ONS1 RINEX data, **b** original ONSA and ONS1 RINEX data

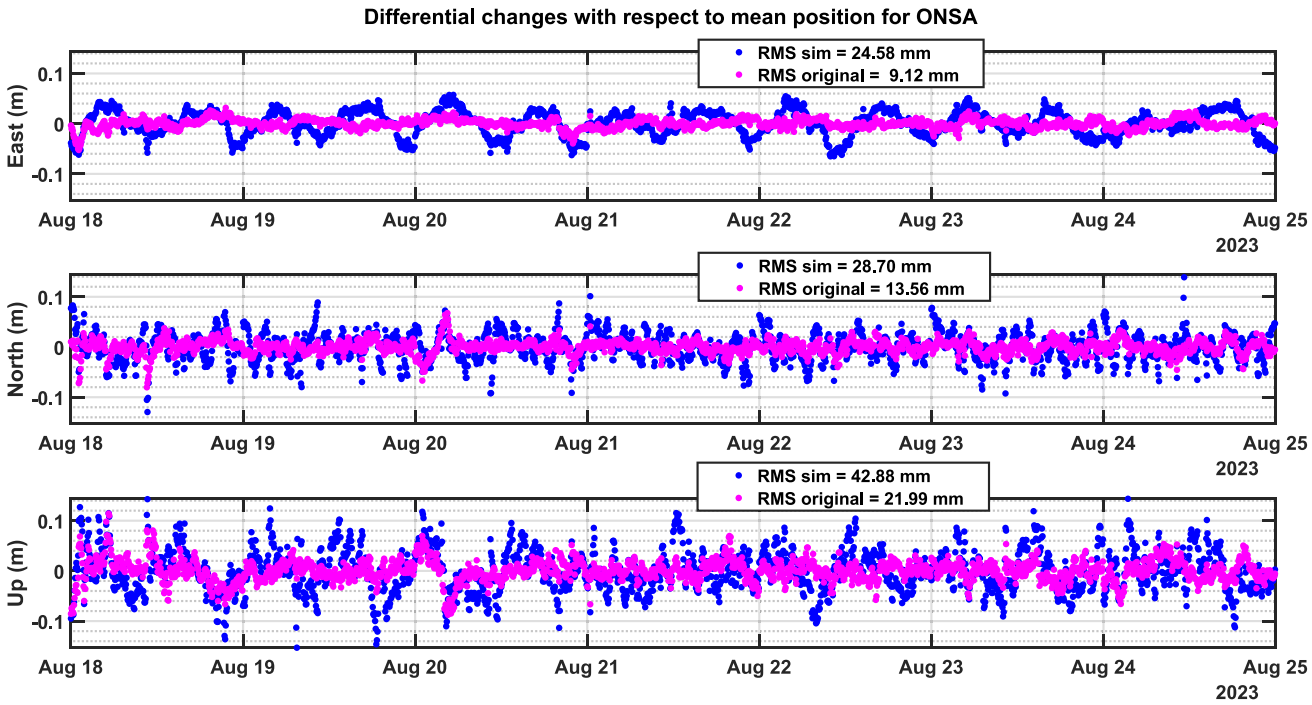

Fig. 5 Time series of relative ONSA east, north and up components in meter with respect to mean position estimates computed using GipsyX PPP processing with GPS and Galileo data

cause much larger and rapid deviations in position. In this case such sudden deviations of position estimates in the north and up component of up to a few decimeters in an absolute sense can be easily noticed in Fig. 5. These instances are short lived but can potentially be serious for a real-time high-precision application. For example in an RTK setup, diffraction impacting the reference station can cause even larger estimation errors on the rover side. These figures act as a reference and one can predict what can be expected from real measurements.

Table 3 summarizes the root-mean-square (RMS) deviations computed for the differential position estimates of ONSA with original or modified RINEX file shown in Fig. 5. Degradation of position estimation by a factor of 2 or even more is noted. However, this is in a worst case scenario with a simulated wall at a constant horizontal distance of 1 meter corresponding to an elevation mask of more than 40^{o}. Future work will focus on controlled experiments to understand the possibility of signal reception at this receiver geometry.

3.2 Studies with real data obtained from the POS1–POS2 baseline

The overriding aim of this study was to investigate diffraction effects on GNSS observations using real data. Therefore, controlled experiments were performed in a rather complicated environment on the roof of a building where significant diffraction effects could be expected. Three different indicators were used to identify diffraction effects in the collected GNSS data, (a) residuals from single-frequency double-difference processing, (b) position estimates using PPP and (c) signal-to-noise ratio of observations. The computations of path delay are verified using geometrical measurements from Lidar scanning around the antenna. The processing steps are same as that of Sect. 3.1. In the following section we describe the experiment setup and the data analysis.

Table 3 RMS deviations of GipsyX PPP estimates of ONSA with 5-minute temporal resolution with GPS and Galileo data

Coordinate	Using original data RMS (mm)	Using modified data RMS (mm)
East	9.1	24.6
North	13.6	28.7
Up	22.0	42.9

3.2.1 Description of experiments and data processing

A pair of receivers (Septentrio PolaRx5) and antennas (LEICA-AR20) with a baseline length of around 50 m were setup on house 7 and 8 of the RISE office in Borås, Sweden. The setup on house 7 is henceforth referred here as POS1 and is shown in Fig. 6a. The setup on house 8 is referred to as POS2 and is shown in Fig. 6b. House 7 also has permanent installations of other GNSS antennas, the nearest one

(a) (b)

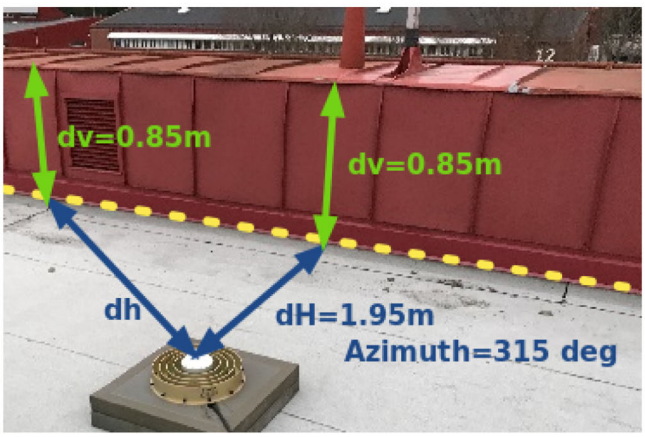

(c)

Fig. 6 **a** Location of POS1 and PRS1 on house 7, **b** location of POS2 on house 8, **c** geometry of the near-by surrounding around antenna POS1

being the one on the left of POS1 as shown in Fig. 6a and will be referred to as PRS1. Figure 6c shows the presence of a metallic wall in the near vicinity of POS1.

It is expected that the POS1 antenna would suffer from obstruction of satellites signals from the north west–north east direction (refer to Fig. 7 for the true north direction), due to the location of the metallic wall. Moreover, there is a possibility of reflection of signals from satellites in the opposite direction. In addition, there are other metallic structures around POS1 as shown in Fig. 6a which might also be the cause of multipath. The occurrence of multipath effects is well established elsewhere in the literature by other authors and other experiments. However, the most interesting part of the POS1 installation is that there is the availability of signals from satellites that should in an ideal situation be blocked by the wall. The possible reason is due to the bending of signals over the edge of the wall demonstrating the presence of diffraction.

Figure 7 provides a clear picture of the relative positions of all four stations POS1, POS2, PRS1 and SPT0. Table 4 summarizes the information about the three stations used in the data processing and also provides the baseline length for all these stations with respect to POS1. As is apparent from the table and also Fig. 6a and b, the POS1–POS2 baseline has the advantage of using antenna and receivers of the same kind with similar installations. This advantage is demonstrated in Sect. 7.1. Therefore, this paper primarily discusses the results from this baseline.

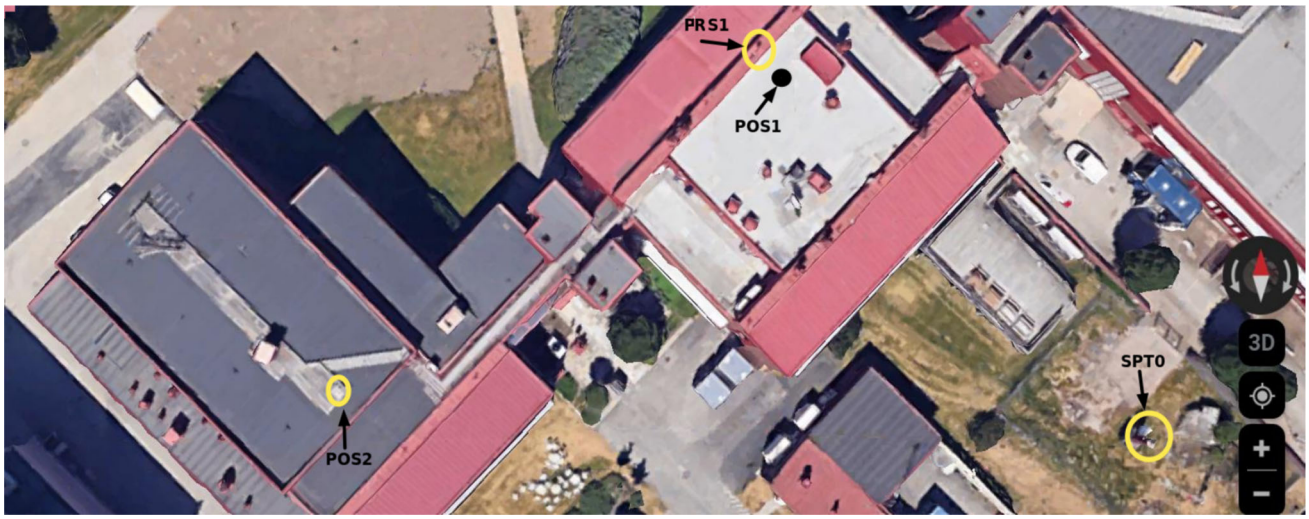

Fig. 7 Screenshot from google maps showing the top view of all the four stations POS1, PRS1, POS2 and SPT0. The north direction is indicated by the arrow on the right side in the figure

Table 4 Station information for the three stations used for the data processing

Station name	Receiver type	Antenna type	Radome type	Baseline length[1]
POS1	Septentrio PolaRx5	LEICA-AR20	–	–
POS2	Septentrio PolaRx5	LEICA-AR20	–	50.459
PRS1	Trimble NETR9	TRM29659.00	SCIS	3.513

Baseline lengths in meters measured with respect to POS1

3.2.2 Post-processing to obtain range residuals for POS1–POS2 baseline

The post-fit residual results presented in this document are processed using high rate clocks provided by the Centre for Orbit Determination (CODE) analysis center which have an update rate of 30 s. Thus the residuals were estimated at 30-second interval. The RINEX files were post-processed using the BSW version 5.4 and the GipsyX GNSS software version 2.3. Single-frequency GNSS observables were used to compute the BSW double-difference residuals for the POS1–POS2 baseline. However, PPP processing using BSW or GipsyX uses dual-frequency measurements to compute the L_3 combination at 300-second sampling rate. The data processing technique is summarized in Fig. 3.

Double-difference residuals were generated with a constrained model (fixed coordinates, no atmospheric estimations) to prevent the absorption of diffraction errors by other parameters (Sect. 3.1.2). Since POS1 and POS2 were temporary GNSS installations imitating typical user-grade receiver setups, their reference coordinates had to be determined prior to any further analysis. To estimate the coordinates, initial PPP processing using the Bernese software with an elevation cutoff (elmin) of 20° was performed for data obtained during June 29–August 17, 2023. The average of these results over the observation period was used as the final (reference) coordinate estimates. The obtained reference coordinates were then kept fixed for a network solution between POS1 and POS2 using the Bernese software and an elevation cutoff of 3° this time. The first residuals obtained from the BSW network processing are used to demonstrate the diffraction effect.

Figures 8 and 9 depict the single-frequency post-fit double-difference residuals from BSW using GRE data on the first and second frequency, respectively, obtained from 40 days of data during the study period. The colormaps shown in these figures have been filtered to remove noisy data by binning the azimuth-elevation space into bins of size 1° by 1° and computing a mean residual per bin. The figures demonstrate clear repeatability of the diffraction effect. The black line at the lower right and left corner of each plot shows the locus of all points that correspond to the top of the metallic wall shown in Fig. 6c. In an ideal situation, a complete absence of data points below the black line is expected due to the blockage by the wall and a consequent shadowing of signal in the region. However, residuals as large as 1 decimeter in the region are computed by BSW. This clearly indicates that there is a signal bending effect due to diffraction.

The results in Figs. 8 and 9 show plots of variation of path length differences over different azimuth and elevation around the receiver antenna. This is similar to the path length differences shown in Table 1 computed using an azimuth

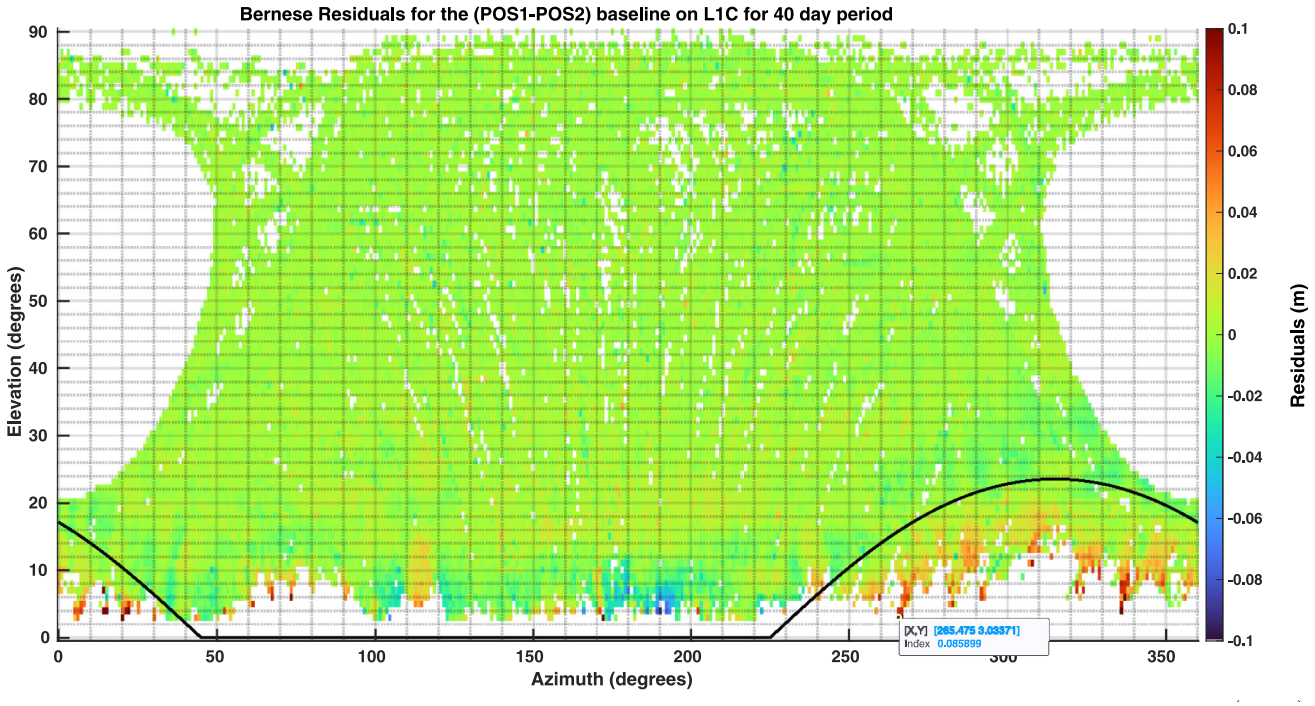

Fig. 8 BSW double-difference residuals for the POS1–POS2 baseline for the first frequency (L1C) observable over 40-day period using GRE data

dependent d. The order of the values for the path length differences obtained from the residuals match the theoretical values shown in Table 1. For example, a path length difference of around 90 mm for an elevation (θ_o) of 3° can be computed at an azimuth of 265° ($d = 3.03$ meter) using the model of Fig. 1a which is also noticed in Fig. 8 as seen in the data tip included in the plot. The impact of diffraction worsens, which is as expected, if the receiver moves closer to the wall.

The plotted residuals in Figs. 8 and 9 are derived from double differences across the POS1–POS2 receiver pair and a satellite pair. Following the convention established in Sect. 3.1.2, the visualization in these figures presents the double-difference data referenced to a specific base pair: receiver POS1 and the second satellite.

3.2.3 PPP position estimates of POS1

The RINEX files of POS1 for the period of June 30–July 15, 2023, were used to compute 5-minute position estimates using PPP analysis with the GipsyX software. GPS, GLONASS and Galileo dual-frequency (L1C-L2W, L1C-L2P, L1C-L5Q) observations with 300-second sampling rate were used for this processing. Position solution using an elevation cutoff of 3° was computed.

Figure 10 shows the time series of station positions with respect to mean position estimates for POS1 in the east, north and up direction, respectively using 3° elevation cutoff. The corresponding RMS values are provided in the figure legends. One can see the impact on position estimations when using low-elevation data that are affected by signal diffraction due to the wall. The processing with 3° elevation cutoff is affected by diffraction as expected. This definitely results in coordinates occasionally being off by more than 5 cm in the east component and up to 12–15 cm in the north and the up component. Some prominent examples that can be pointed at are the position estimates computed at around 17:40 on 6 July and at 19:55 on 11 July. These instances are short lived but can potentially be serious for a real-time high-precision application. While a 5-minute position update rate was used, a faster rate could increase the visibility of diffraction impacts in the position estimates as more satellite passes would be affected. However, this would also introduce higher measurement noise, potentially obscuring diffraction as the dominant error source.

The frequent gross errors in positioning due to diffraction, as shown by the sudden jumps in the position estimates (Fig. 10), cause large and rapid deviations in position. Although brief, these events pose a substantial risk to real-time precision. This is particularly critical for RTK, where diffraction at the reference station propagates and amplifies errors at the rover. Figure 10 validates the positioning behavior anticipated in Sect. 3.1.3 (based on Fig. 5).

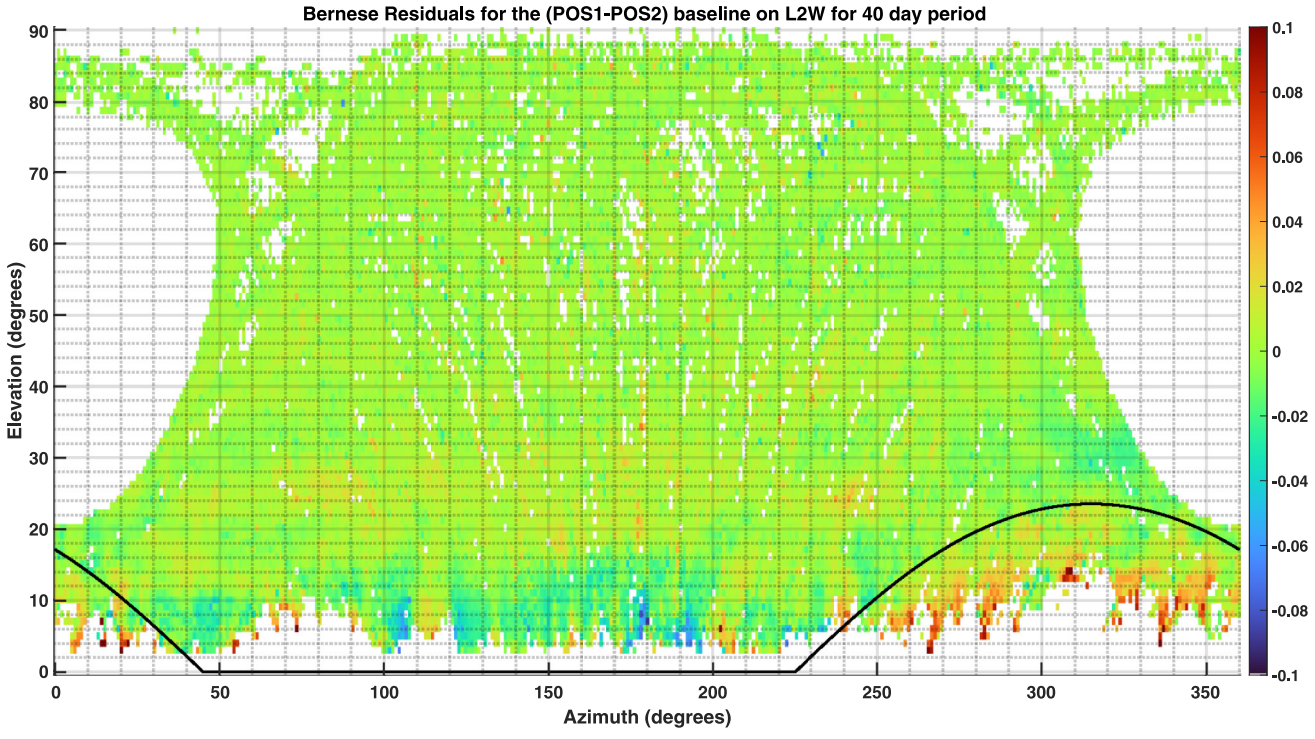

Fig. 9 BSW double-difference residuals for the POS1–POS2 baseline for the second frequency observable over 40-day period using GRE data (GPS-L2W, GLONASS-L2P, Galileo-L5Q)

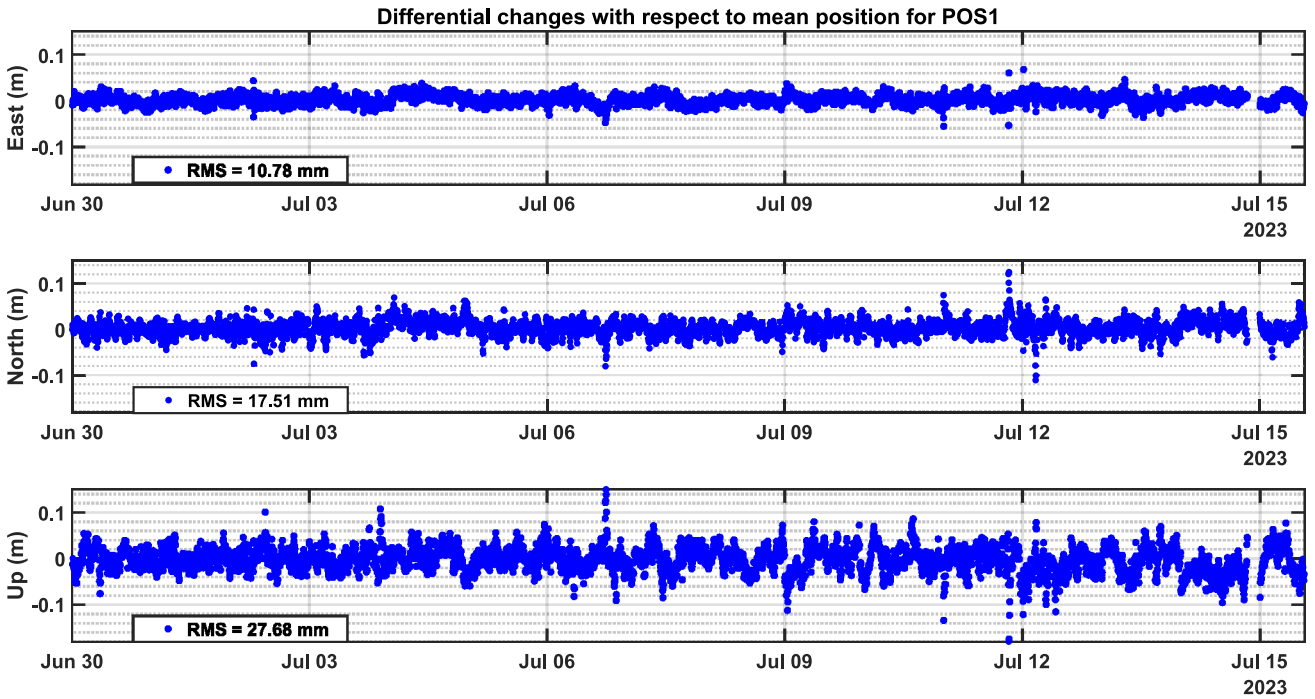

Fig. 10 Time series of relative POS1 east, north and up components in meter with respect to mean position estimates computed using GipsyX PPP processing with GPS, GLONASS and Galileo data

3.2.4 Results at POS1 using signal-to-noise ratio measurements of the GPS L1C signal

The knife edge diffraction model described in Sect. 2.1 using Eq. 6, was used to compute an approximate of the expected diffraction loss. The value of ν was computed using Eqs. 7, 8 and 11 for different values of azimuth and elevation. The geometrical measurements for the environment around POS1 are as shown in Fig. 6c. Thus, a set of values of loss L were obtained at different azimuth and elevation. It is expected that if a signal were to face diffraction on its way to the receiver antenna, it would be attenuated by the amount predicted by Eq. 6 for the specific values of ν which in turn depends on the geometry of the receiving environment. This diffraction loss L was then added to the modeled open sky SNR to determine the composite SNR which is compared with the real SNR data.

Following the approaches of Zhang and Hsu (2021) and Suzuki and Kubo (2012), a long-term, open sky SNR model for POS1 was developed. The model, which expresses SNR as a function of satellite elevation, was derived from a 59-day dataset of 1-second RINEX observations for GPS satellite G05 (as an example) and is presented in Fig. 11. The model is obtained by first-order polynomial fitting of SNR measurements between elevations of 39^o and 55^o. A linear regression fit, for various reasons, is not the perfect way of modeling open sky SNR. However, we are interested in the diffraction modeling on SNR, and the open sky model is only needed as a basis to add the diffraction effects to. Similar open sky models were derived for other example GPS satellites G06, G08, G15 and G16 in the given azimuth range. The diffraction loss computed using Eqs. 6 to 9 at every epoch was then added to the corresponding open sky SNR model for the respective satellite. Figure 12 shows the plots of observed/measured and modeled SNR variations for all these satellites in the vicinity of the wall.

The satellite track as seen at POS1 was computed using CODE SP3 files (Center for Orbit Determination in Europe 2023) and is shown in Fig. 12 together with the measured and modeled SNR. To get a clear picture, also a curve for the variations of elevation of the wall with respect to azimuth has been added. Please note that for the subplots of Fig. 12, the vertical axis on the left shows elevation and corresponds to the plot of the wall and the satellite track, while the vertical axis on the right shows SNR and corresponds to the scatter of the measured or the modeled SNR. One can see from Fig. 12 that signals are still received at very low elevations even behind the wall which is possible only if there is signal bending at the wall edge. The modeled SNR together with the diffraction loss fits well with the real measured values with a maximum residual deviation of 7 dB-Hz. This demonstrates that the signal degradation is due to diffraction and not multipath. The diffraction impact is seen for all the satellites that go behind the wall in the specific azimuth range of the wall as is clear from Fig. 12.

Further, one can see from Fig. 13 that the impact is even larger for the less robust S2W signal on the L2 frequency. A sudden drop in signal strength by at least $15 - 20$ dB is noted in every case when the satellite track encounters the wall. The worst case signal strength drop is really large and signals get registered even at low elevations in the shadow region of the wall. Please note that G16 is an old satellite of Block-II-R generation launched in 2003 with lower SNR in the S2W channel compared to the other satellites.

3.2.5 Quantitative evidence of diffraction as the dominant signal degradation mechanism—validation using a single satellite

The local environment on the roof of house 7 is a complicated environment, and the POS1 installation site was purposefully selected to reflect the suboptimal conditions commonly faced by a typical GNSS end user, thereby enhancing the relevance of this study. While the occurrence of multipath around the vicinity of the GNSS antenna cannot be eliminated, this section is aimed at demonstrating the presence of diffraction alone using Lidar point cloud measurements generated using Leica GS 18 and Lidar scanner ZF 5010X. The software Cyclone 3DR (Leica Geosystems AG (2024)) was used for processing the Lidar point cloud. We use the position of a single satellite, for example GPS satellite G05, at a certain azimuth to demonstrate this. However, the process remains the same for all other satellites in the given azimuth. Please refer appendix Sect. 7.2 for numerical details of the position information, etc. The satellite, receiver and other [x,y,z] coordinate positions mentioned in Sect. 7.2 and here are in ITRF20 reference frame and given in meters. Computations in this section clearly show that at certain azimuth, the signal arriving at the POS1 antenna is due to bending caused by diffraction alone and not due to multipath. The computations are verified with the actual values of obtained residuals and the theoretical values shown in Table 1.

Figure 14 shows the Lidar point cloud around the POS1 antenna installation. All blue lines in the figure merge at the position of POS1. The light blue line shows the direction to North. The dark blue lines show arrival of GNSS signals from different directions. On the right side of POS1 across the images is the metallic wall. Figure 14a shows the complete picture with the wall and the PRS1 antenna mount, and Fig. 14b shows a close up.

As is clear from Fig. 12, GPS satellite G05 encounters the wall at azimuth 304^o. The satellite position is given in Sect. 7.2. One can compute elevation and azimuth using SP3 files for the satellite position, and it is seen that on 23-Aug-2023 the encounter with the wall occurs between UTC 14:56:50 and 15:32:20. Specifically for the epoch,

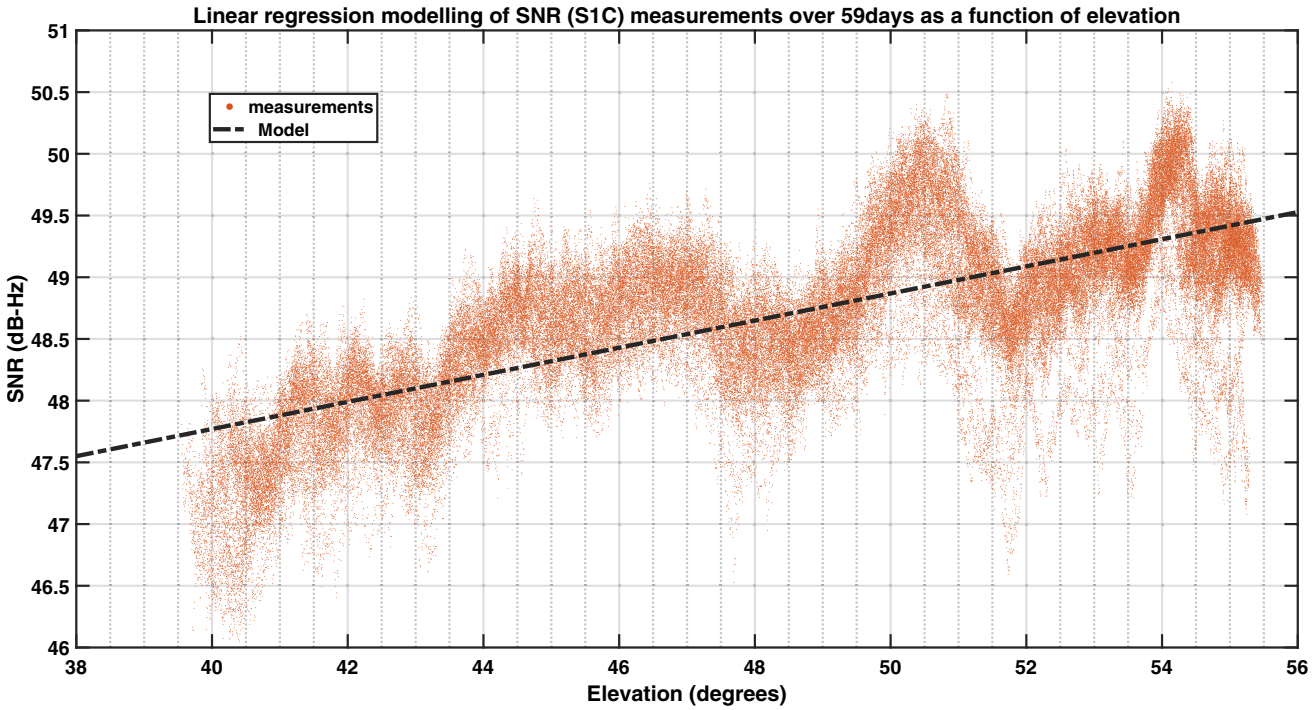

Fig. 11 Linear regression model of the open sky S1C signal measurements for GPS satellite G05 over 59 days

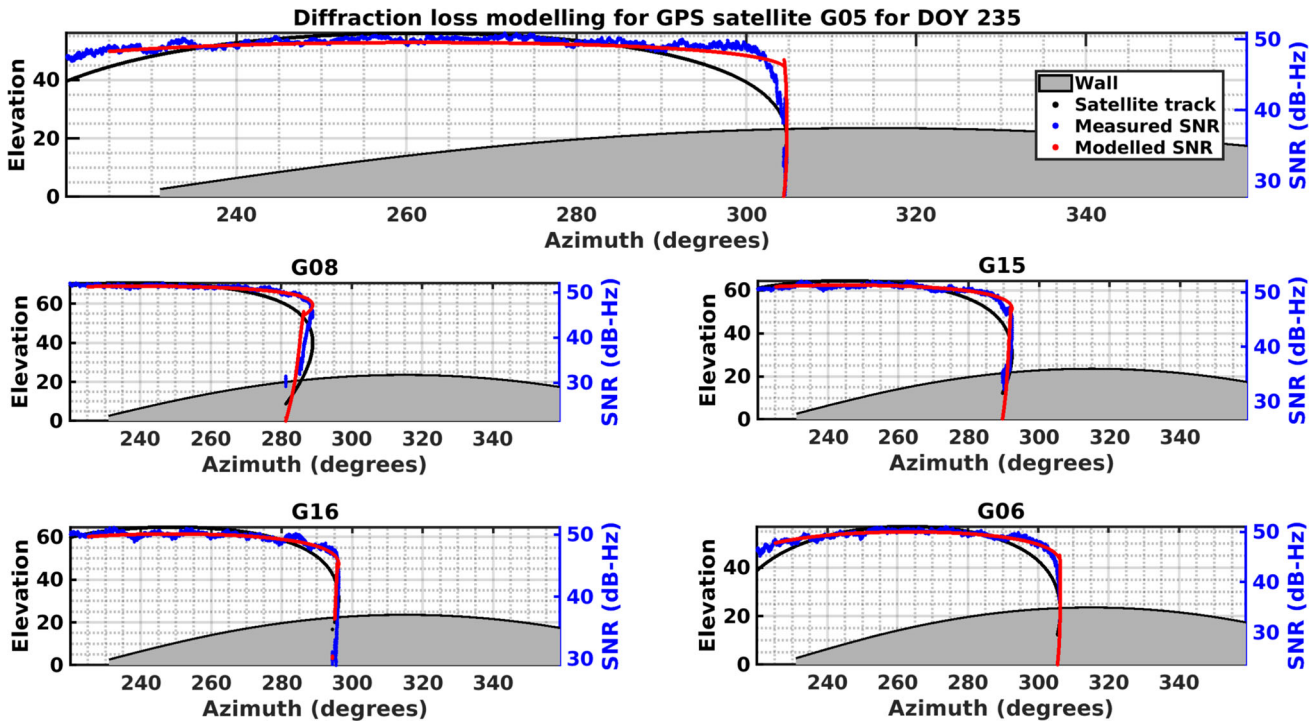

Fig. 12 SNR modeling for various GPS satellites on the S1C channel for DOY 235

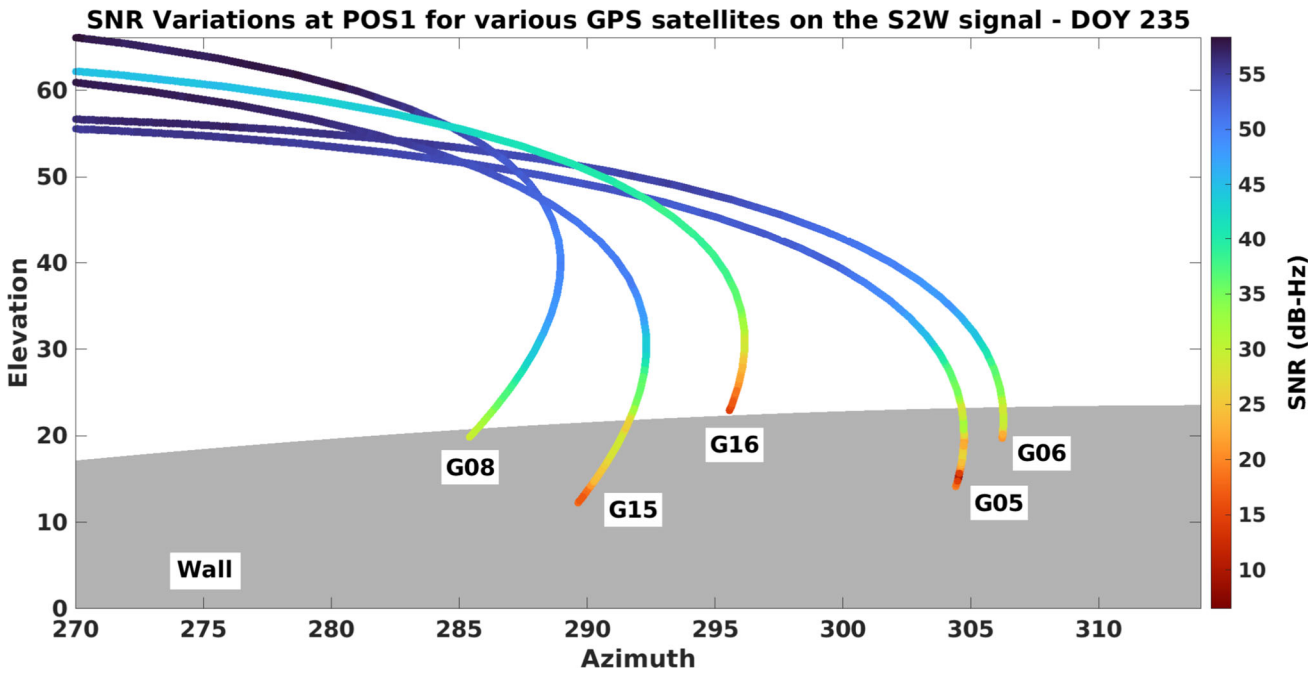

Fig. 13 SNR variations for S2W signal for all GPS satellites in the given azimuth range show clear indication of signal degradation when the satellites meet/ are behind the wall

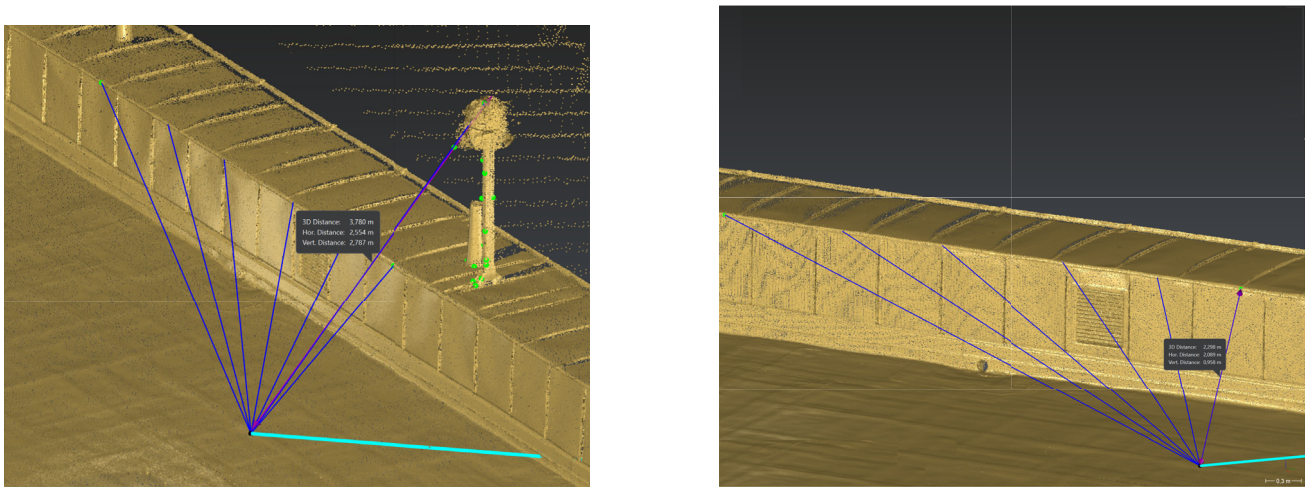

(a) With PRS1 and POS1

(b) Zoomed in to show only POS1

Fig. 14 Lidar point cloud around the POS1 antenna installation. All blue lines merge at the position of POS1. The light blue line shows the direction to North. The dark blue lines show arrival of GNSS signals from different directions. On the right side of POS1 across the image is the metallic wall. On top of the wall is the PRS1 antenna mount

'2023-08-23 15:00:00', the satellite is behind the wall. POS1 coordinates obtained using the procedure followed in Sect. 3.2.2 are given in Sect. 7.2. A point of arrival of the satellite signal at around azimuth 304^{o} on the wall is also given in Sect. 7.2. It is easy to compute the path length for the SGP from the satellite to POS1, and this is 24038740.9715 meter. The SGP length from the satellite to the point on the wall is 24038738.7186 meter. Using Lidar measurements, the point on the wall is at a slant distance of 2.29 meter from POS1 as shown in Fig. 14b. Thus it can be computed that, if the signal were to bend at this point on the wall and arrive at the receiver, then an extra path length of 0.037 meter is encountered by the bent/diffracted signal.

This can further be verified using the theoretical computations shown in Table 1. The point on the wall is located at a horizontal distance d of 2.1 meter. From the table one

can estimate that at this distance at an elevation of $12-14^{o}$ (which is roughly near the elevation of the satellite) the delay due to signal bending is about $2-3$ centimeter, which is inline with our computations.

Finally, let us have a closer look at the double-difference residuals for G05 and G15 for August 23, 2023. G15 is another satellite that encounters the wall at azimuth 292^{o}.

Figure 15 plots the data shown in Fig. 8 but for satellites G05 and G15 over the 40-day period. The different colors in the plot indicate residuals of the respective satellites for different days over the 40-day period. Each residual point belongs to a different double-difference pair that includes either G05 or G15; the plot aggregates data from multiple such pairs. Please note that while a direct G05-G15 pair may exist within the dataset, the figure is not exclusively only for that pair. It is essential to recognize that the large positive scatter of residuals at azimuth 292^{o} and 304^{o} is due to the satellites G15 and G05 encountering the wall at these azimuth. The residual values from these figures clearly point to similar amount of path length difference as computed by us earlier in this section. The observed path length difference is attributed to signal bending at a specific point on the wall, indicating that, at this azimuth, the signal received is solely due to diffraction. Also, as pointed out in Sect. 3.2.4, the modeled SNR together with the diffraction loss fits well with the real measured values for satellite G05. This configuration effectively rules out the presence of multipath as a major interferer at this particular angle. However, as previously discussed, the potential for multipath effects at other azimuthal orientations cannot be excluded. In some cases, a combination of diffraction and multipath may also be present. Future research by the authors will aim to deepen the understanding of signal propagation via diffraction and to systematically assess the environmental and observational conditions under which such phenomena are registered.

4 Discussion

Precise positioning techniques, whether PPP or baseline processing, are vulnerable to unmodeled local errors that do not cancel in the estimation. Signal diffraction is one such site-specific effect that can degrade accuracy at a single station. PPP accuracy relies on the comprehensive modeling of GNSS error sources. While standard PPP accounts for systematic errors like orbits and clocks, it does not automatically correct for local, unmodeled effects such as signal diffraction. When diffraction occurs, the PPP estimator absorbs the error by biasing other parameters—in this case position estimates—leading to the erroneous solutions shown in Figs. 5 and 10. The impact is most severe when the obstacle is nearer to the receiver (1 meter in the case of ONSA-ONS1 baseline) and diminishes with distance (1.95 meter in the case of POS1–POS2 baseline with real data).

Analyzing diffraction requires an approach distinct from standard PPP. The ionosphere-free (L_3) combination used in PPP is unsuitable for quantifying this wavelength-dependent phenomenon. A more effective method is single-frequency analysis using double-differenced data from co-located receivers. The residuals shown in Figs. 4a, 8 and 9 directly indicate the diffraction impact caused by the obstacle.

These double-differenced residuals are a function of a receiver pair (POS1, POS2) and a pair of satellites at each epoch. Given that the POS2 station serves as an error-free reference, its contribution to the residuals is considered negligible. Consequently, the residuals are dominated by errors originating from the POS1 receiver and the diffracting obstacle. When the obstacle is simulated at 1 meter, it is expected to cast a large shadow on the antenna, causing a significant number of satellite signals to be diffracted. At a distance of 1.95 meters, the obstacle casts a smaller shadow, affecting fewer satellites in the POS1–POS2 baseline. With the obstacle farther away, signals from lower-elevation satellites become visible and are subject to diffraction. It remains to be inspected, however, until what elevation signals would be visible in real data for the 1 meter case. We intend to report this in our future work.

Analysis of Signal-to-Noise Ratio (SNR) variations offers valuable insight into the physics of signal diffraction. This study utilizes L1C signal data from multiple GPS satellites to examine this phenomenon. In our case, the knife edge model works well for showing the diffraction impact. But it may not be perfect for all scenarios with obstructions of finite dimensions and non-ideal "knife edge" properties. We plan to improve the model in our future work.

The geometry of diffraction is characterized by the relative height (h) and the normalized Fresnel diffraction parameter (ν), derived from Eqs. 7 and 8. As shown in Fig. 1a, the value of h indicates whether the direct path is obstructed ($h > 0$), grazing the obstacle ($h = 0$) or clear ($h < 0$). The parameter ν synthesizes the height, wavelength (λ) and obstacle distance into a single, dimensionless value that determines the extent of Fresnel zone intrusion. While $\nu = 0$ also implies grazing incidence, the range from -1 to 0 is the most interesting. It is at this point that the satellite has a clear line of sight, and yet, since the obstruction already perturbs the first Fresnel zone, the signal strength attenuates sufficiently. This will be studied in detail in our future work.

It is expected that an obstacle that is very close will cause more satellites to have their first Fresnel zone completely or partially blocked. This will interfere not only with PPP position estimation, as explained earlier, but will also be clearly visible in the network solution. Essentially, the closer the obstruction of a constant height, the greater the diffraction impact. This finding contrasts with the theoretical derivation

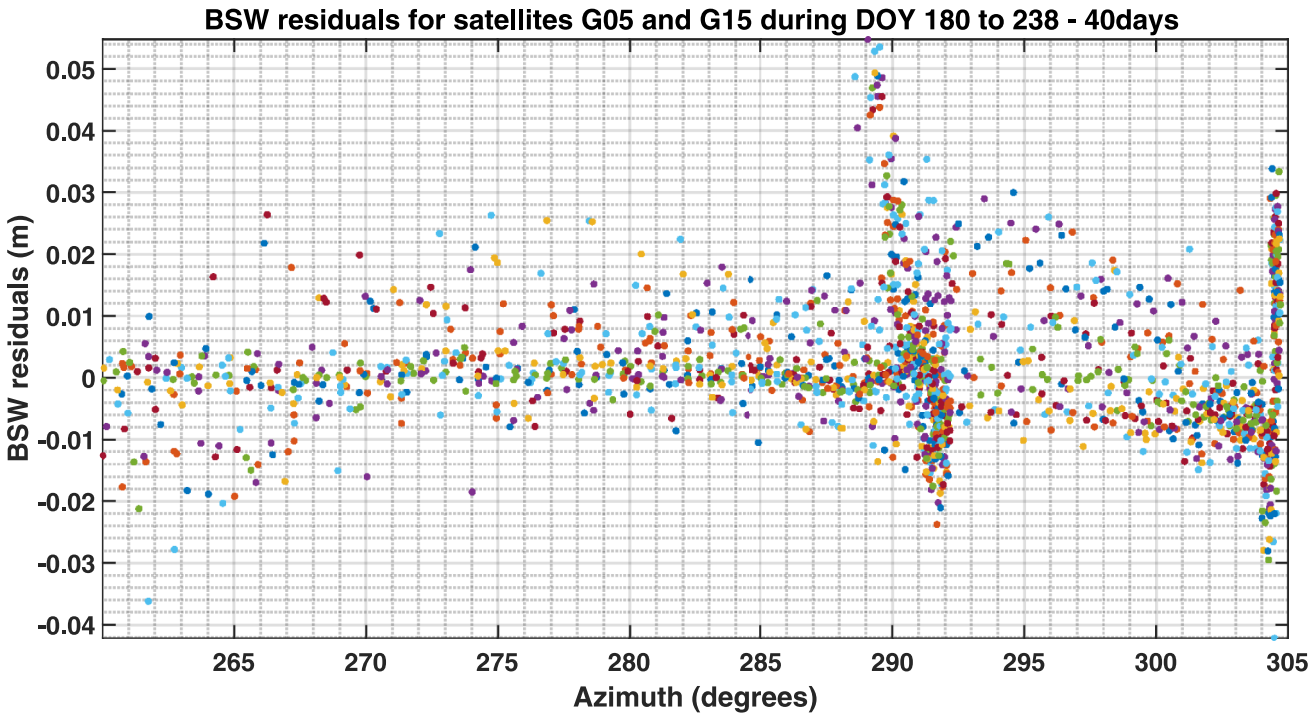

Fig. 15 BSW double-difference residuals for satellites G05 and G15 as obtained for 40-day data

of Xi et al. (2025), who suggest a larger diffraction error with increasing distance (S, analogous to d in this study). This discrepancy may arise if they implicitly assume an obstacle whose height increases proportionally with distance—a scenario uncommon in practical applications but interesting for a theoretical understanding. Also, if the geometry of the obstacle changes proportionately, then at some point it would block more than the first Fresnel zone. It would be interesting to understand if their theory remains valid when the obstacle is in the second Fresnel zone.

Furthermore, the assertion by Xi et al. (2025) that diffraction error could be larger at high elevations is not supported by our data. Low-elevation satellites, when visible, are consistently more affected, as evidenced by the larger residuals at lower elevations in Figs. 4a, 8 and 9. However, any satellite with a disturbed first Fresnel zone will experience interference, which is a direct hindrance to precise positioning. Therefore, it is important to quantify the distance at which an obstruction ceases to be a significant diffractor—for example, to determine a safe distance from a wall. More controlled experiments are being performed, and the results from these will be detailed in our follow-up work.

5 Conclusions

GNSS carrier phase and SNR measurements are visibly and quantifiably affected by diffraction from an obstruction like a wall, even when the satellite has a direct line-of-sight. Diffraction introduces a slowly varying, systematic bias into the measurements, which degrades the accuracy of high-precision positioning. The error is deterministic and structured, meaning it cannot be averaged out and requires physical or empirical modeling. While not studied in this paper, we think that like position estimates, unmodeled diffraction may get absorbed into estimated tropospheric parameters, posing a problem for atmospheric studies. Moreover, diffraction compromises the integer nature of carrier phase ambiguities, leading to fix failures or biased "fixed" solutions. Also, excellent satellite geometry with low Dilution of Precision (DOP) can coexist with large, systematic errors, demonstrating that in the presence of diffraction, DOP is a necessary but not sufficient condition for high accuracy(Dutta and Johansson 2023). For geodetic-grade applications, the antenna environment must be free not only of obstructions but also of near-grazing diffracting edges. The 1.95 meter distance wall experiment is a perfect example of a problematic feature that would be present in many real-world IGS installations (example on a building parapet). A single such affected station can introduce biases that propagate into a larger geodetic network solution, affecting the products for all users. Over decades, this small bias can translate into a significant positional error, degrading the reference frame and compromising studies such as crustal deformation, sea-level rise and post-glacial rebound.

It is observed from simulation results that position estimation can get twice as worse or even more in the presence of non-minimal diffraction effects. Impact of diffraction is clearly visible in the BSW double-difference residual plots both in the simulated and the real data. PPP processing using dual-frequency ionosphere-free (L_3) combination amplifies existing uncertainties that make it more difficult to isolate the effect of diffraction. In order to demonstrate such an effect, single-frequency analysis using a network of co-located stations is recommended. In addition use of similar receiver antenna setup is always advantageous.

In real-time high-precision GNSS applications usually an elevation cutoff angle of 10^o to 15^o is applied. The user, e.g., in machine guidance applications, depends on GNSS data every second. Since there are often many surrounding objects, including the machine itself, multipath and diffraction are frequently occurring. In many real-time situations, the effect of these problems will become more serious than described in this paper since our results are based on post-processing in a controlled environment. In the best case these problems will cause lost lock and/or cycle slips (resulting in an alarm signal to the driver), but a potentially more serious effect is incorrectly estimated coordinates at the several centimeter-level or even decimeter-level. For moving or even rotating road work machines such as excavators and cranes, the problems of multipath are well known. Diffraction is a problem that is either unknown or possibly known but disregarded. The appearance of the problem is short-lived, but in an RTK setup, diffraction impacting the reference station can cause even larger estimation errors on the rover side. This can potentially be serious and limiting the achievable measurement uncertainty in RTK and NRTK (Network RTK) applications.

As a future work, we will focus on assessing the conditions where diffraction signals are registered. Analysis with critical height computations on real data collected from new experiments in a more controlled environment will be carried out. The role of Fresnel zone computations will be investigated in detail. Simple strategies such as cleaning data of the diffracted satellites will be investigated as a first step to mitigate diffraction effects. However, it is expected that cleaned data can also have worse positioning estimates compared to original data due to availability of less number of satellites in certain epochs resulting in poor DOP. Therefore removing affected satellites may not be the best strategy in all cases. Other strategies of diffraction mitigation using machine learning will also be investigated.

7 Appendix

7.1 Triple differences to test quality of POS1–POS2 baseline measurements

In this section we explain how we used triple differences to analyze the quality of the measurements in the POS1–POS2 baseline. As is already well known, for a cycle slip free satellite arc, epoch difference solution by triple differencing removes most major error sources such as atmosphere, orbits, satellite and receiver clock errors and also the ambiguities (Ogaja 2024). Even the phase windup effect if any should be taken care of by an epoch difference solution, since the residual is a difference between two consecutive epochs. Thus the triple-difference residual should primarily consist of errors related to the local environment or the receiver phase center variations and the ever present random receiver noise. A cross-correlation between epoch difference residuals of two consecutive days would determine if these solutions have a larger random noise component or a larger repeatable component. If the correlation is perfect between two sidereal days, the residual has a larger component due to the local environment in case of a static antenna, since GPS exhibits sidereal day repeatability. Thus there is minimal receiver noise and other random receiver-related effects that impact the baseline. Such a baseline then produces quality measurements which can be used to isolate the diffraction impact. However, if the correlation is imperfect between epoch difference solutions of two consecutive days, the residuals from such a baseline carry more of the randomness from the receiver noise and thus use of such a baseline to pull out diffraction effects is not optimal. It is recommended to avoid the use of such baselines for carrying out the analysis explained in Sects. 3.1.2 and 3.2.2.

RINEX data collected during June 29th–August 26th, 2023 (DOY 180-238), with sampling interval of 1 s were used for the analysis using triple differences. Triple differences on the L1C observable for the POS1–POS2 baseline for a cycle slip free arc of the GPS satellite pair G03 and G04 and are shown in Fig. 16. The advantage of performing triple differences is that even ambiguities are eliminated if the receivers did not lose lock within the time interval and no cycle slip occurred (Dach et al. 2015). Atmospheric errors are considerably mitigated on the triple-difference level for the co-located POS1–POS2 baseline (Ogaja 2024). The difference in Figs. 16 and 17 is also related to the longer baseline between POS1 and POS2, and we observe the residual part

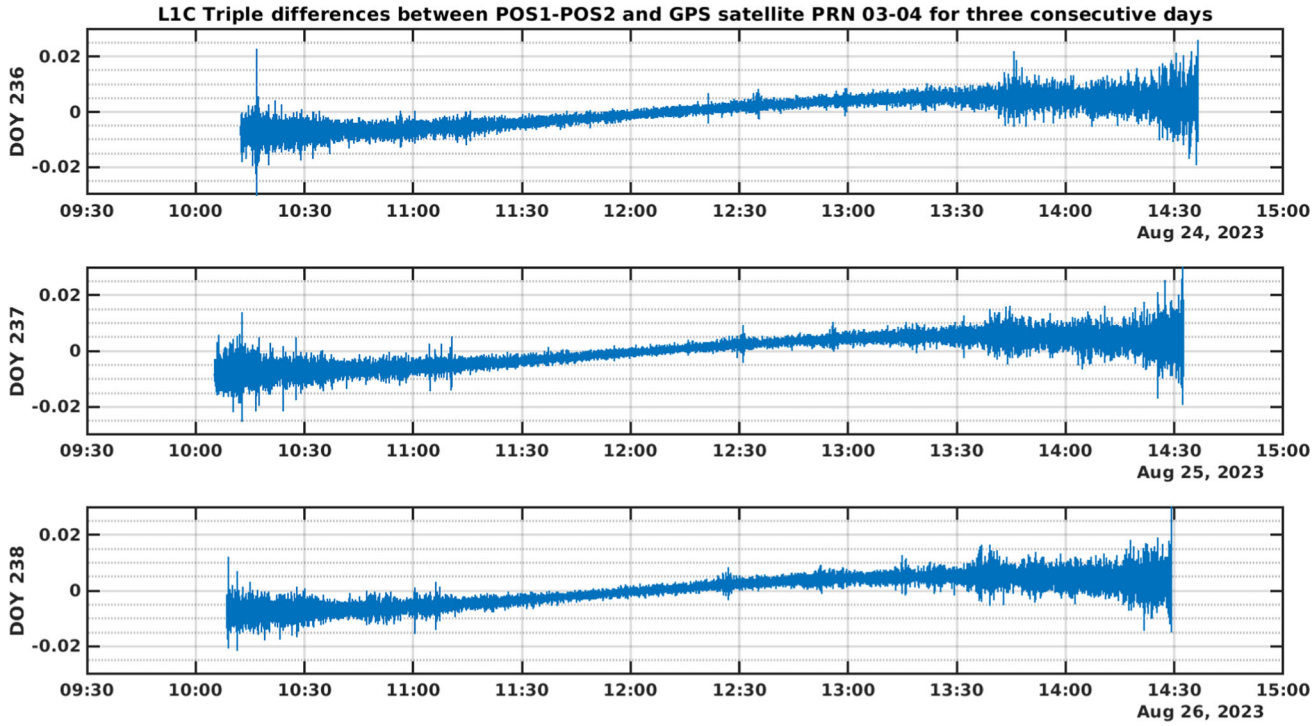

Fig. 16 Triple differences computed for the POS1–POS2 baseline using GPS single-frequency observable L1C over a cycle slip free arc demonstrate sidereal day repeatability over 3 consecutive days

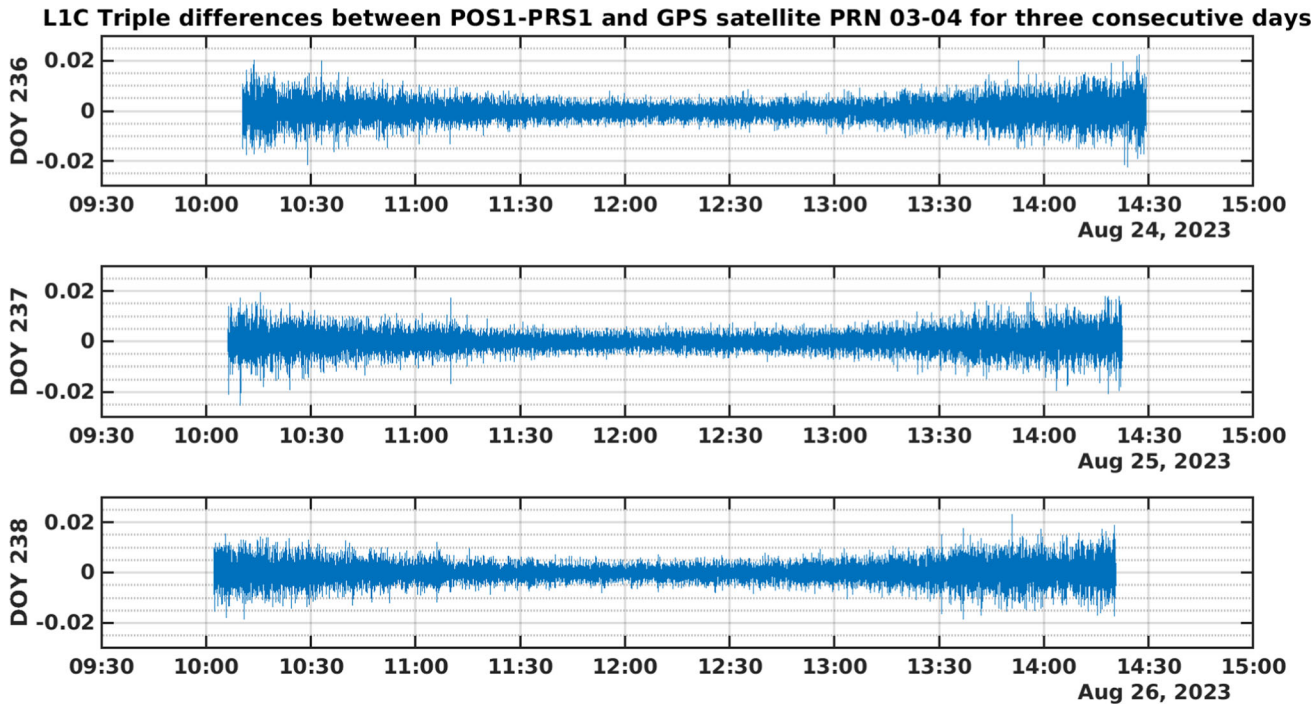

Fig. 17 Triple differences computed for the POS1-PRS1 baseline using GPS single-frequency observable L1C over a cycle slip free arc demonstrate sidereal day repeatability over 3 consecutive days

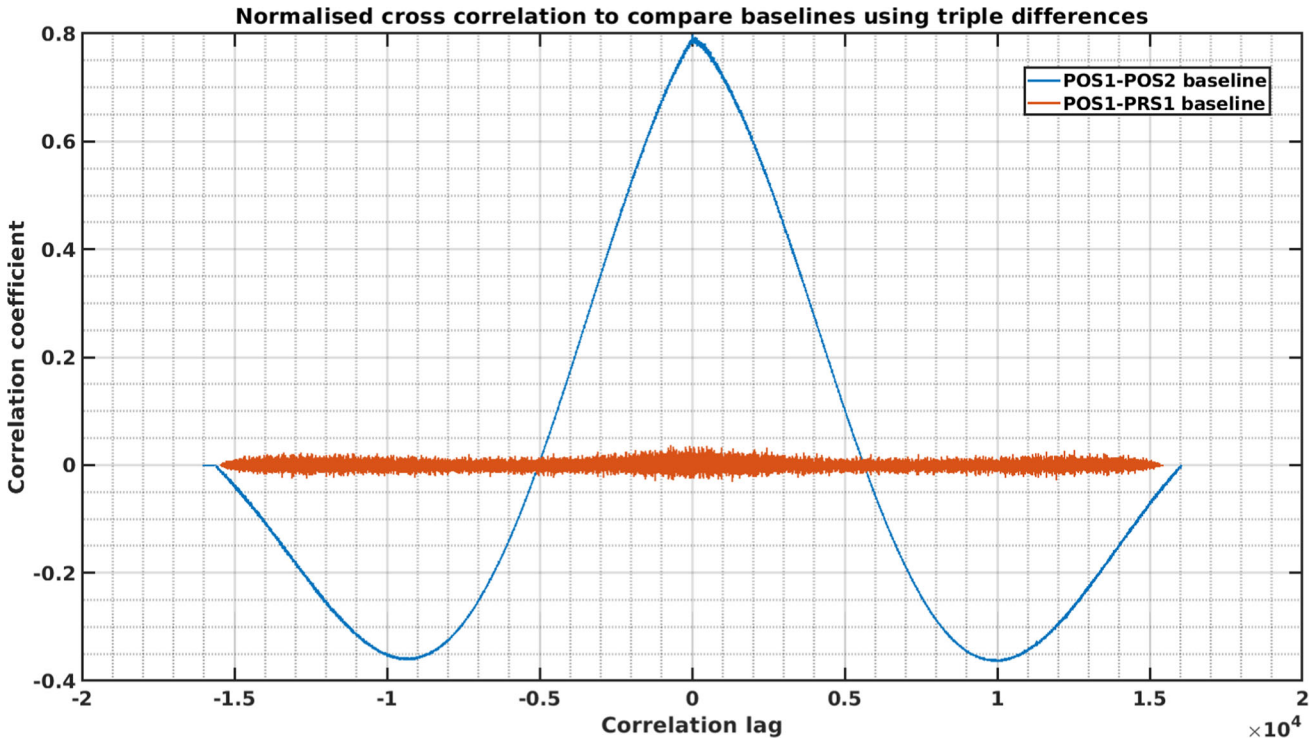

Fig. 18 Normalized cross-correlation of triple differences of two consecutive days (aligned by shifting the data of second day by the sidereal day difference) for the POS1–POS2 baseline in blue and the POS1-PRS1 baseline in red

Table 5 Summary of Key Positions and Path Lengths

Satellite position (2023-08-23 15:00:00 UTC)	[3586.723, −19 621 882.45, 17 669 692.23] m
Receiver position (POS1)	[3 328 966.1403, 761 866.8966, 5 369 054.7749] m
SGP length to POS1	24 038 740.9715 m
Wall Interaction point	[3 328 966.3125, 761 865.0067, 5 369 056.0566] m
Slant distance from POS1	2.29 m
SGP length from satellite to wall point	24 038 738.7186 m
Excess path length—due to diffraction	0.0371 m

of the triple differenced geometrical distance as a slow trend in Fig. 16. However, as explained before, the major part of the triple-difference residual are errors due to local unmodeled effects such as those due to the environment of the antenna, but it can also be attributed to the antenna themselves. There is also a component of receiver noise in the residuals. While the effects due to the environment should be correlated between consecutive days, since the antenna is static, the receiver noise constitutes the uncorrelated part. Triple differences for three consecutive days during August 24 to 26, 2023, for POS1–POS2 baseline are shown in the Fig. 16 to demonstrate their sidereal day repeatability. L1C triple differences for the POS1-PRS1 baseline are also computed for three consecutive days during August 24 to 26, 2023, and are shown in Fig. 17.

Figure 18 shows the normalized cross-correlation results of two consecutive days for the POS1–POS2 and the POS1-PRS1 baseline. Clear correlation between two-day data of the POS1–POS2 baseline shown in Fig. 18 indicates that the POS1–POS2 baseline is quite free of other equipment-related effects. This could be attributed to the fact that POS1 and PRS1 use different kind of antenna and receiver. The residuals in POS1–POS2 baseline primarily point to local unmodeled error sources that exhibit correlation over two side real days since the environment can be assumed static over two days.

7.2 Numerical details for path delay computation

The satellite, receiver and other [x,y,z] coordinate positions mentioned here are (Table 5) in ITRF20 reference frame.

Acknowledgements The authors acknowledge the support of Trafikverket for the funding provided through the Stomnät i Luften (SiL 2.0) project grant number TRV 2018/111087, 2019. The authors also acknowledge the support of colleagues from RISE - Carsten Rieck for providing access to data from PRS-1, etc., and Sten Bergstrand for helping in accurately setting up the POS1 installation. Finally, the authors would like to acknowledge the support from the GEO group of the Dimension and Position unit, Mätteknik department at RISE for the Lidar scanning, especially Magnus Herbertsson.

Author contributions The individual contributions of the authors are as follows: U.D. contributed to overall conceptualization, methodology, investigation, data curation, validation, formal analysis, visualization, writing—original draft, writing—review & editing. **J.J.** was involved in resources, supervision, writing—review & editing. **R.H.** contributed to conceptualization (of simulation studies), writing—review & editing. All authors have read and agreed to the published version of the manuscript.

Funding Open access funding provided by Chalmers University of Technology. This work is part of a PhD project funded by RISE Research Institutes of Sweden.

Data availability The data that support the findings of this paper are available upon reasonable request.

Materials Availability Not applicable.

Code availability The software code for generating the findings of this paper is available upon reasonable request.

Declarations

Conflict of interest No Conflict of interest.

Ethical approval Not applicable.

Consent for publication Yes.

References

Altamimi Z, Rebischung P, Collilieux X et al (2023) ITRF2020: an augmented reference frame refining the modeling of nonlinear station motions. J Geodesy 97:47. https://doi.org/10.1007/s00190-023-01738-w

Bertiger W, Bar-Sever Y, Dorsey A et al (2020) GipsyX/RTGx, a new tool set for space geodetic operations and research. Adv Space Res 66(3):469–489. https://doi.org/10.1016/j.asr.2020.04.015

Bradbury J (2007) Prediction of urban GNSS availability and signal degradation using virtual reality city models. In: Proceedings of the 20th International Technical Meeting of the Satellite Division of The Institute of Navigation (ION GNSS 2007), Fort Worth, TX, September 2007, pp. 2696–2706

Breitsch B, Morton YT, Rino C et al (2020) GNSS carrier phase cycle slips due to diffractive ionosphere scintillation: Simulation and characterization. IEEE Trans Aerosp Electron Syst 56(5):3632–3644. https://doi.org/10.1109/TAES.2020.2979025

Brunner FK, Hartinger H, Troyer L (1999) GPS signal diffraction modelling: the stochastic SIGMA-δ model. J Geodesy 73(5):259–267. https://doi.org/10.1007/s001900050242

Center for Orbit Determination in Europe (CODE) (2023) CODE final product series for the IGS. Astronomical Institute, University of Bern, ftp://ftp.aiub.unibe.ch/CODE/

Dach R, Andritsch F, Arnold D, et al. (2015) Bernese GNSS software version 5.2. DOI: 10.7892/boris.72297

Dutta U, Johansson J (2023) Multi-constellation/Multi-frequency GNSS signal degradation due to foliage and reflective environments. Eng Proc. https://doi.org/10.3390/ENC2023-15454

Fan K, Ding X (2006) Estimation of GPS carrier phase multipath signals based on site environment. J Global Pos Syst 5:22–28. https://doi.org/10.5081/jgps.5.1.22

Groves PD, Adjrad M (2017) Retracted article: Likelihood-based GNSS positioning using los/nlos predictions from 3d mapping and pseudoranges. GPS Solutions 21(4):1805–1816. https://doi.org/10.1007/s10291-017-0654-1

Groves PD, Jiang Z (2013) Height aiding, C/N0 weighting and consistency checking for GNSS NLOS and multipath mitigation in urban areas. J Navig 66(5):653–669. https://doi.org/10.1017/S0373463313000350

Hofmann-Wellenhof B, Lichtenegger H, Wasle E (2008) GNSS - Global Navigation Satellite Systems: GPS, GLONASS, Galileo, and more. Springer, Vienna, Austria, https://link.springer.com/book/10.1007/978-3-211-73017-1

IGS (2025) Supporting the ITRF. https://igs.org/itrf/

International GNSS Service (IGS) (2018) RINEX: The Receiver Independent Exchange Format Version 3.04. RINEX Working Group and RTCM-SC104, available at https://files.igs.org/pub/data/format/rinex304.pdf

Jiang Z, Groves PD (2014) NLOS GPS signal detection using a dual-polarisation antenna. GPS Solut 18(1):15–26. https://doi.org/10.1007/s10291-012-0305-5

Leica Geosystems AG (2024) Leica Cyclone 3DR. https://leica-geosystems.com/products/laser-scanners/software/leica-cyclone/leica-cyclone-3dr, version used: 2024.0

McGraw GA, Groves PD, Ashman BW (2020). Robust positioning in the presence of multipath and NLOS GNSS signals. https://doi.org/10.1002/9781119458449.ch22

Nicolás ML, Smyrnaios M, Schön S, et al. (2012) Investigation of diffraction effects in GNSS using ray tracing channel modelling: Preliminary results. In: 2012 6th European Conference on Antennas and Propagation (EUCAP), pp 3154–3158, DOI: 10.1109/EuCAP.2012.6206167

Ogaja C (2024). An Introduction to GNSS Geodesy and Applications. https://doi.org/10.1007/978-3-031-74494-5

Orfanidis SJ (2002) Electromagnetic Waves and Antennas. Rutgers University, New Brunswick, NJ, http://leipper.org/manuals/zip-fill/www.ece.rutgers.edu/~orfanidi/ewa/ch17.pdf

Panicciari T, Soliman MA, Moura G (2017) Evaluation of a GNSS receiver performance in different multipath environments with a novel real-time multipath simulation system. In: Proceedings of the 30th International Technical Meeting of the Satellite Division of The Institute of Navigation (ION GNSS+ 2017), Portland, Oregon, pp 427–435, 10.33012/2017.15199

Rappaport TS (1996) Wireless Communications: Principles and Practice, 1st edn. Prentice Hall, Upper Saddle River, NJ

Ren H, Li G, Geng J et al (2023) Multipath hemispherical map model with geographic cut-off elevation constraints for real-time GNSS monitoring in complex environments. GPS Solut. https://doi.org/10.1007/s10291-023-01530-5

Schaper A, Ruwisch F, Schön S (2022) Diffraction modeling for improved 3DMA GNSS urban navigation. In: 35th International Technical Meeting of the Satellite Division of the Institute of Navigation, ION GNSS+ 2022, pp 1902–1916, 10.33012/2022.18541

SMHI (2025) Smhi weather. https://www.smhi.se/klimat/klimatet-da-och-nu/hur-var-vadret/q/Bor%C3%A5s/precipitation

Suzuki T, Kubo N (2012) GNSS positioning with multipath simulation using 3d surface model in urban canyon. In: 25th International Technical Meeting of the Satellite Division of the Institute of Navigation 2012, ION GNSS 2012 1:438–447

Xi R, Xu D, Jiang W et al (2023) Elimination of GNSS carrier phase diffraction error using an obstruction adaptive elevation masks determination method in a harsh observing environment. GPS Solutions 27(3):139. https://doi.org/10.1007/s10291-023-01473-x

Xi R, Han L, Chen Q et al (2025) Numerical modeling and analysis of GNSS carrier-phase diffraction error in occlusion environments. J Geodesy 99(4):32. https://doi.org/10.1007/s00190-025-01956-4

Zhang G, Hsu LT (2021) Performance assessment of GNSS diffraction models in urban areas. Navigation 68(2):369–389. https://doi.org/10.1002/navi.417

Zhang Z, Li Y, He X et al (2022) A composite stochastic model considering the terrain topography for real-time GNSS monitoring in canyon environments. J Geodesy 96:79. https://doi.org/10.1007/s00190-022-01660-7

Zimmermann F, Eling C, Kuhlmann H (2017) Empirical assessment of obstruction adaptive elevation masks to mitigate site-dependent effects. GPS Solut 21(4):1695–1706. https://doi.org/10.1007/s10291-017-0650-5

Zou X, Fu R, Tang J et al (2023) Multipath error mitigation method considering NLOS signal for high-precision GNSS data processing. GPS Solutions 27(4):175. https://doi.org/10.1007/s10291-023-01498-2

Uttama Dutta is a researcher at RISE Research Institutes of Sweden in the department of Measurement Science and Technology. She received a Licentiate degree in 2024 from Chalmers University of Technology, Sweden, and is presently pursuing a PhD in the unit of Space Geodesy and Geodynamics at the same university. Her research focuses on enhancing the reliability of GNSS carrier phase measurements for precise positioning applications. In particular, she investigates GNSS error sources such as ionosphere and antenna environment.

Jan Johansson is a researcher at RISE Research Institutes of Sweden and adjunct Professor of Space Geodesy at Chalmers University of Technology. He is the director of the Swedish National Metrology Institute (NMI) hosted at RISE and the Swedish representative in the international metrology community. His research interest focuses on space geodetic techniques and applications of Global Navigation Satellite Systems (GNSSs).

Rüdiger Haas is a Full Professor of Space Geodesy at Chalmers University of Technology. He is the Head of the Research Group for Space Geodesy and responsible for the geoscience activities at the Onsala Space Observatory. His research interests focus on space geodetic techniques, such as Global Navigation Satellite Systems (GNSSs), including GNSS reflectometry, and very long baseline interferometry (VLBI).